Fluid-dynamics of the 1997 Boxing Day volcanic blast on Montserrat, W.I.

T. Esposti Ongaro[1], A. B. Clarke[2], A. Neri[1], B. Voight[3], C. Widiwijayanti[3]

[1]Istituto Nazionale di Geofisica e Vulcanologia, Sezione di Pisa, Italy
[2]Dept. of Geological Sciences, Arizona State University, USA
[3]Dept. of Geosciences, Penn State University, USA

Abstract. *Directed volcanic blasts* are powerful explosions with a significant laterally-directed component, which can generate devastating, high-energy pyroclastic density currents (PDCs). Such blasts are an important class of eruptive phenomena, but quantified understanding of their dynamics and effects is still incomplete. Here we use 2D and 3D multiparticle thermofluid dynamic flow codes to examine a powerful volcanic blast that occurred on Montserrat in December 1997. Based on the simulations, we divide the blast into three phases; an initial burst phase lasts roughly 5 s and involves rapid expansion of the gas-pyroclast mixture, a gravitational collapse phase which occurs when the erupted material fails to mix with sufficient air to form a buoyant column and thus collapses asymmetrically, and a PDC phase which is dominated by motion parallel to the ground surface and is influenced by topography. We vary key input parameters such as total gas energy and total solid mass to understand their influence on simulations, and compare the simulations with independent field observations of damage and deposits, demonstrating that the models generally capture important large-scale features of the natural phenomenon. We also examine the 2D and 3D model results to estimate the flow Mach number and conclude that the range of damage sustained at villages on Montserrat can be reasonably explained by the spatial and temporal distribution of the dynamic pressure associated with subsonic PDCs.

1. Introduction

Directed volcanic blasts are powerful explosions with a significant laterally-directed component, which can generate devastating, high-energy pyroclastic density currents. Volcanic blasts have had violent consequences at Bezymianny, Russia, in 1956 [Belousov, 1996], and Mt. St. Helens, USA in 1980 [Hoblitt et al., 1981; Moore and Sisson, 1981; Waitt, 1981; Fisher et al., 1987; Fisher, 1990; Druitt, 1992]. They represent an important and extremely hazardous class of eruptive phenomena, and consideration of blasts and their associated pyroclastic density currents (PDCs) is necessary for modern volcanic hazard zonation at stratovolcanoes [Crandell and Hoblitt, 1986]. However, quantified prediction of their dynamics and effects is still possible only at a generalized level, often involving simplifying assumptions, such as one- or two-dimensional, steady, and/or choked flow [e.g., Kieffer, 1981; Woods et al., 2002].

The term "*directed volcanic blast*" was suggested for the first time by Gorshkov [1959], who studied the eruption of Bezymianny volcano in Kamchatka in 1956. This directed blast was observed only from large distances, and thus the main conclusions about mechanisms of the event were based on interpretations of the effects and deposits of the eruption. The very similar explosive eruption of Mount St. Helens in 1980 [Lipman and Mullineaux, 1981] rekindled a worldwide interest in directed blasts, and the mass and variety of observations, monitoring data, photo-documentation, and detailed geologic studies at Mount St. Helens enabled a quantum improvement in understanding of the basic causative mechanisms. It was observed that the large-scale collapse of the volcanic edifice, which transformed into a debris avalanche, was the event that triggered a directed explosion by suddenly exposing a pressurized body of magma and gas to atmospheric pressure [Voight, 1981; Voight et al., 1981, 1983; Glicken, 1998]. This explosion, and the pyroclastic density current that it generated, devastated a large area of complex topography and left deposits closely resembling those of Bezymianny [Hoblitt et al., 1981; Moore and Sisson, 1981; Waitt, 1981; Kieffer, 1981; Walker and McBroome, 1983; Brantley and Waitt 1988; Fisher et al., 1987; Fisher, 1990; Druitt, 1992; Sisson, 1995; Bursik et al., 1998; Belousov et al., 2007].

Through deposit studies and field observations, it has been generally recognized that an initially-pressurized lava dome or cryptodome, suddenly depressurized by a slope failure, can create a directed blast. However, controls on the strength, direction and physics of the initial explosion, its subsequent transformation to a PDC, and propagation of the PDC across incised volcanic topography, require further analysis, with 3D analysis required to capture full interaction with topography. This capability has been lacking in the past in computational fluid dynamics modeling of explosive volcanic phenomena.

The recent directed blast from the Soufrière Hills volcano (SHV), Montserrat, provides the opportunity to further improve our understanding of blast dynamics. This blast and associated PDC eradicated the village of St. Patricks and substantially damaged much of the southern part of the island, on 26 December (Boxing Day) 1997 (Figures 1, 2). In this case, despite the severity of the event, no lives were lost because a pre-emptive evacuation was enforced, based on recognition of flank instability and the anticipation of a blast [Young et al., 2002]. The resulting deposits and destructive effects have been well studied [Sparks et al., 2002; Ritchie et al., 2002; Voight et al., 2002; Baxter et al., 2005], and thus despite certain limitations, and apart from the images recorded uniquely at Mount St. Helens, the database for this event is unsurpassed for eruptions of this type.

Here we perform a preliminary study using a 2D cylindrical-coordinate model, which allows us to efficiently parameterize the effect of the initial dome mass and energy on the blast behavior and to constrain appropriate initial conditions for later implementation in the 3D model. We then apply a fully 3D multiphase flow model incorporating realistic 3D topography, using initial conditions constrained by field observations. We compare these runs against the field observations of the Montserrat event, in order to demonstrate broad-scale similarity between natural phenomena and our model results. We also use the 3D results to demonstrate relationships between the flow dynamics and initial conditions, topography, spatial location, and time, within the context of the model assumptions.

The effects of gas compressibility and shock waves on the eruption dynamics was first investigated by Nairn [1976] and Nairn and Self [1978] for vertical explosions. Some authors modeled the directed blast at Mount St. Helens as a quasi-steady-state overpressured, supersonic jet, accompanied by internal shock structures and compressibility effects [Kieffer, 1981, 1984; Kieffer and Sturtevant 1984, 1988; Wohletz and Valentine, 1990]. Here, we use *directed blast* simply to denote an explosion, caused by decompression of a cryptodome or lava dome, with a significant initial lateral component and an asymmetric deposit distribution due to an asymmetric source geometry and/or edifice morphology. A contested question is whether the preponderance of strong damage observed in volcanic directed blasts should be attributed to air shocks [Wohletz et al., 1984; Wohletz 1998], supersonic flow within an overpressured jet [Kieffer 1981, 1984], or flow dynamic pressure [Sparks et al., 2002; Baxter et al., 2005; Esposti Ongaro et al., 2005] and (possibly) shocks within the energetic collapse and PDC (gravity current) phases. Exploring this issue is an additional goal of this paper.

2. Observational constraints on the Boxing Day blast

At Soufrière Hills Volcano (SHV) in December 1997, an andesite dome and talus cone with a volume of 113 × 10^6 m^3 was growing above the hydrothermally altered and unstable south flank of the volcano. Gravitational collapse of the flank on 26 December triggered an explosive decompression of the dome's interior, to form a violent blast and PDC that traveled >4 km overland, and then continued >3 km over the sea surface [Voight et al., 2002; Sparks et al., 2002; Hart et al., 2004]. The volume of material (dense rock equivalent, DRE) involved in the failure was estimated from the dimensions of the failure scars and by comparison with pre-collapse topography [Sparks et al., 2002; Voight et al., 2002]: c. 20-30 × 10^6 m^3 from the south flank hot spring area, c. 5 × 10^6 m^3 from the old crater rim, c. 25 × 10^6 m^3 from the lava dome that had grown between 6 November and 26 December, and about 30 × 10^6 m^3 of lava talus. We take the volume of dome lava participating in the blast as ~25 × 10^6 m^3 (DRE), exclusive of additional materials that may have been incorporated through erosion. The lava volume is relatively well constrained, but the volume of entrained material is not well constrained due to offshore deposition [Hart et al., 2004]. The total duration of strong activity was ~11.6 min but occurred in several pulses. The volatile components in the blast came from the andesite, and the material comprising the blast was a complex multiphase vapor-liquid-solid mixture.

Seismic data suggest 6 pulses [Sparks et al., 2002], and stratigraphy reveals clearly only two depositional events, and at least two erosional events resulting from relatively large pulses [Ritchie et al., 2002]. Thus two seismic events are not accounted for in the stratigraphy. It is possible they were both largely erosional onshore or perhaps early deposits were eroded by later pulses, leaving no record observed on land. The individual pulses were short lived, lasting but a few minutes. Only 2-3 × 10^6 m^3 DRE was deposited on land with the remainder entering the sea or elutriated by co-PDC plumes. Our constraints are poor but we estimate the small pulse volumes to be ~1 to 5 × 10^6 m^3 DRE, with the minimum value bounded by the volume per pulse deposited on land. The large pulses were two or three times the volume of the small pulses, based on seismic magnitudes, with the sum of all pulses being about 25 × 10^6 m^3 DRE plus eroded and entrained materials. Co-PDC plumes reached a height ~15 km asl, with two separate parts, an ash-rich upper part, and an ash-poor lower part rich in condensed steam [Pace et al., 1998; Mayberry et al., 2002]. The latter is inferred to be a consequence of the PDC entering the sea. The airborne ash was about 15-20% of the original PDC volume [Sparks et al., 2002].

The area devastated on land was ~10 km^2 with some pulses affecting a 70^o sector and a much smaller pulse depositing mainly over only a 35^o sector (Fig. 2). The damage varied from complete destruction in the central axial region, to lesser physical effects such as blown out windows and roofs, and fire damage, in peripheral areas [Sparks et al., 2002; Baxter et al., 2005]. The destruction was complete in the axial area of the blast near the village of St. Patricks where structures were razed to their foundations, with detached structural components (including building walls) flattened to the ground or carried to the sea along with loose debris. Buildings swept away include stone-built structures and those with poured reinforced concrete walls. Trees with trunks up to 1m in diameter were removed entirely leaving only abraded stumps and roots [Sparks et al., 2002]. Entrained boulders and pieces of destroyed buildings added to the destructive capability of the PDCs in addition to dynamic pressure [Baxter et al., 2005]. East of the axial area of the blast zone and the White River valley, the blast zone is dominated by erosional features across the raised shoulder of an older volcanic edifice. The severity of damage decreases systematically, but with local variability, from the axis of the PDC towards the lateral periphery. One kilometer west of the axial zone, the top floors of houses were blown down and scattered 50 m down slope, impact marks from saltating boulders occur on house walls facing the volcano, and trucks and a bulldozer were flung over a cliff onto the beach [Sparks et al., 2002; Baxter et al., 2005]. Although trees up to 50 cm in diameter were broken a few meters above ground, smaller trees (<10 cm trunks) and shrubs were merely bent over with branches stripped and the trunk tip sharpened by abrasion. Still farther from the axis, house walls were damaged, roofs were partially or entirely removed, and cars were crumpled and displaced tens of meters. At the western lateral limit of damage, 200-m from source, damage was limited to in-blown windows and displaced roof tiles and blown-down wooden sheds [Sparks et al., 2002]. Dynamic pressures estimated from the damage ranged from >25 kPa in the central axial region to 1-3 kPa near the periphery, with local fluctuations of about ~1-5 kPa associated with localized sheltering and topographic effects [Baxter et al., 2005].

There are several other constraints on the dynamics of the Boxing Day event. The upper part of the current climbed almost to the summit of South Soufrière Hills (SSH), from the saddle between Galways Mountain and South Soufrière Hills [Fig. 2; Sparks et al., 2002]. The trimline representing the upper surface of the current descends the side of Galways Mountain to the saddle at about 600 m a.s.l., where the current collided with the South Soufrière Hills and climbed 150 m further. Converting kinetic to potential energy for the height climbed in the Galways-SSH peripheral zone results in 55 m s^{-1} for the upper part of the current in this region [Sparks et al., 2002].

A reliable but limited constraint on dynamics is given by the St Patricks seismic station, MSPT, about 3.4 km from the dome [Voight et al., 2002; Sparks et al., 2002]. The initial collapse began about 03:01.0 LT (the signal is emergent, making it difficult to pick onset time), the first stronger seismic pulses began at 03:01.8 LT and 03:02.8 LT, respectively, and MSPT was destroyed at 03:03.3 LT [Sparks et al., 2002]. If one assumes that the blast pulse that destroyed MSPT began during the first seismic pulse, the implication is that average frontal speeds were 38-56 m s^{-1}. An alternative interpretation is that the first seismic pulse represented mainly edifice collapse and debris avalanche movement, and that the second, sharp, seismic pulse represented the blast initiation. This interpretation yields an average frontal blast velocity of 113 m s^{-1}. Nevertheless, focusing exclusively on *average* velocities could be misleading since modeling presented here and observations at SHV [Sparks et al., 2002] and Mount St Helens [Voight, 1981; Moore and Rice, 1984; Hickson, 1990; Hoblitt, 2000; Belousov et al., 2007] illustrate that velocities were not constant. We therefore discuss temporal and spatial distribution of blast characteristics from both an observational and modeling perspective later in the text.

Dynamic pressure estimates for the pyroclastic density current presented above [Sparks et al., 2002] were calculated from building damage following the approach of Valentine [1998a], where dynamic impact pressures in pyroclastic currents were compared with pressures required to damage structures in atomic explosions. The dynamic pressure P_d is half the product of current mixture density and velocity squared, so that velocity can be calculated if current density is known. Sparks et al. [2002] assumed a mass fraction of gas in the flow and calculated a current density of 6 kg m^{-3}. Using this density, about five times that of ambient air, they concluded that maximum velocities could have been ~30-40 m s^{-1} in the peripheral area near Kinsale, >40 m s^{-1} near Germans Ghaut, and >>60 m s^{-1} at St. Patricks.

3. Blast modeling

Previous steps toward conceptual and quantified understanding of directed blast behavior illuminated many features of the phenomenon. For example, the lateral blast at Mount St. Helens was modeled as a horizontal quasi-steady-state, underexpanded, supersonic jet with perfect coupling between gas and solid phases [Kieffer, 1981]. These results found limited support in numerical simulations by Wohletz and Valentine [1990], who also explored shock effects in vertical explosions. For Montserrat, modeling of decompression and dome fragmentation [Woods et al., 2002] were combined with an analytical 1D ash-flow model to illustrate basic controls on runout distance and dynamic pressure of the directed blast [Sparks et al., 2002]. Here we assume the model of lava dome pressurization presented by Woods et al. [2002], and apply 2D and 3D unsteady multiphase models of pyroclastic dispersal to the rapid decompression of that dome.

Our approach builds upon that of Woods et al. [2002] and effectively extends it in several ways. First, flow in volcanic blasts is highly unsteady and the source conditions are reported to be impulsive. We therefore calculate the rapid decompression of a lava dome with finite mass and gas energy, which creates an impulsive source for our blast model. Second, we relax the assumption of perfect coupling between the gas and solid phase (pseudogas assumption) and thus treat the multiphase aspects of the blast (discussed in the model section below). The perfect coupling assumption is reasonable only for particles ≤30 microns in diameter [Woods, 1995; Neri et al., 2003], while recent work synthesizing deposit data shows that ~88% of directed-blast clasts exceed 30 microns [Belousov et al., 2007]. Furthermore, high acceleration in the initial phases of blasts is likely to produce high levels of decoupling between solid and gas phases. Both conditions make relaxing the pseudogas assumption desirable and potentially important. Third, we treat the system in 3D allowing the effects of complex topography on flow propagation to be explicitly explored. In a directed-blast the exposed vent and lava- or cryptodome geometry direct much of the momentum at angles highly oblique to the vertical [Voight, 1981; Belousov et al., 2007]. Moreover, flow channeling and azimuthal variations in topography have particular importance in evolution of the flow [Belousov, 1996; Hoblitt et al., 1981; Ritchie et al., 2002]. Evidence of flow channeling at distances from the vent greater than several km was observed at SHV [Sparks et al., 2002; Druitt et al., 2002] and Mount St. Helens [Hoblitt et al., 1981; Kieffer, 1981; Waitt, 1981], revealing that channels allowed dangerous flows to move far from the blast axis, and cause destruction in locations that would not necessarily have been predicted by intuition or by 2D simulations. Furthermore, tree blowdown patterns at MSH [Waitt, 1981; Kieffer, 1981] provide evidence of topography-initiated flow separation and formation of large-scale eddies. As a result of rugged topography, damage was highly variable over relatively short spatial scales.

3.1. Physical and numerical model

Motivated by the aforementioned factors, our model describes the dynamics of directed blasts by adopting the multiphase transport theory [Gidaspow, 1994; Valentine

1998b; Dartevelle, 2004]. Accordingly, each phase of the mixture (gas, liquid, and solid with specific characteristics) is described separately from the others by solving the corresponding mass, momentum, and energy balance equations. The model thus describes the kinetic and thermal disequilibrium of the gas and particles, and the interphase momentum and energy exchange. In detail, we adopted the PDAC (*Pyroclastic Dispersal Analysis Code*) code [Esposti Ongaro et al., 2007; Neri et al., 2007], which solves the multiphase flow equations on two and three-dimensional domains with topography imported from a digital elevation model (DEM). This code is an evolutionary advance from the KFIX code developed at the Los Alamos National Laboratory (USA) in the mid 70's [Rivard and Torrey, 1977], and further developed along one evolutionary branch at the Illinois Institute of Technology (US) for fluidization engineering studies [Gidaspow, 1994]. The basic model formulation and algorithm derive from the work of Harlow and Amsden [1975], in which classical iterative methods for subsonic flows were extended to the compressible and supersonic regime and to multiphase flows. The details of these models are given by Neri et al. [2003], Dartevelle [2004], and Esposti Ongaro et al. [2007].

This approach makes it possible to investigate the dispersal of pyroclasts in the atmosphere and along the volcano flanks without the need of *a priori* assumptions and *ad-hoc* parameterizations of the flow features (e.g., the transient 3D feature allows effective description of flow characteristics in the different regions of the system, the turbulent entrainment is explicitly simulated through the large eddies of the flow and only parameterized at the subgrid scale, the particle settling velocity is computed explicitly by the model as a function of flow properties and need not be specified *a priori*). Moreover, the possibility of using different particle classes gives us the opportunity to investigate the different dispersal pattern of each particle size as well as the effect of their relative proportion on the flow behavior.

Nevertheless, several limitations to our model formulation still exist. Present model formulation is limited to solid volume fraction less than about 50 vol.%. Above this threshold, the flow likely enters a frictional regime requiring a different set of constitutive equations. Moreover, although the model describes the sedimentation and stratification within the flow (as well as particle elutriation) through the settling of different particle classes, an explicit deposition model (i.e. particle loss from the ground boundary condition) is not included at this time in the formulation, so that particles are assumed to remain fluidized at all times. A recent study by Dufek and Bergantz [2007] has shown that deposition through a leaky boundary can significantly decrease runout distance, therefore our estimates should be considered liberal in this respect. However, on Montserrat on land, because of the steep slopes there was little deposition and the stronger pulses were erosive. So for the modeling in this paper, the lack of a deposition subroutine seems unimportant. Similarly, erosion and entrainment of substrate material into the density current are not explicitly considered in our model. The thermal interactions between the hot PDCs and the sea surface, and phase changes (condensation) of water vapor, are not specifically treated. However, water vapor condensation is possible only in the upper region of the computational domain, as verified by computing *a posteriori* the water vapour saturation pressure as a function of local pressure, temperature and concentration.

Full model verification and validation is an ongoing endeavor, especially for 3D flows, including "validation" against natural events, with new regimes and dynamic conditions being tested continually. To this aim, several applications of the PDAC code in 2D have been successfully carried out in the last decade to assess the model's ability to capture the behavior of compressible, dilute, turbulent multiphase flows. Neri and Gidaspow [2000] have compared 2D cylindrical and Cartesian model solutions to fluidization experiments in order to test the formulation of the particulate phase. Similarly, the gas turbulence subgrid model has been validated against experiments of gas flow around a bluff-body [Barsotti, 2002]. The accuracy of compressible flow simulations was also tested for both one- and two-dimensional shock tubes and supersonic jets by comparison against analytical solutions and well-validated results obtained by other codes [Esposti Ongaro et al., 2006, 2007]. Clarke et al. [2002a,b] compared solutions of PDAC2D against well-documented Vulcanian explosions on Montserrat in 1997.

3.2 Initial conditions for the multiphase flow model

Initial source conditions are as follows. The dome is represented as a hemisphere on a sloping base with uniform gas volume fraction of 0.1, based on measurements given by Robertson et al. [1998] and Melnik and Sparks [2002]. During the effusive phase, the dome grows as degassed magma reaches the interior or surface of the dome, while the exsolved volatiles separate from the magma and travel through the permeable dome to the atmosphere [Melnik and Sparks, 1999; Sparks et al., 2002]. Models of viscous conduit flow with gas escape show that overpressures of several MPa can develop near the conduit exit, where overpressure is taken as the difference between gas pressure and local lithostatic pressure [Sparks, 1997; Melnik and Sparks, 2002]. The overpressure is only partially dissipated by gas escape through the permeable dome. We use the Woods et al. [2002] permeable hemisphere model to determine initial pressure profiles within the lava dome prior to the blast, for a steady gas (steam) flux of ~400 kg s^{-1} and dome permeability K. The gas flux is consistent with measured magma extrusion rates of ~8 m^3 s^{-1} for December 1997 [Sparks et al., 1998], and bulk volatile content ~2 wt% [Barclay et al., 1998]. No COSPEC measurements were made during December 1997, but this result is conservative with correlated SO_2 flux with magma output, ~680 g SO_2 per tonne of magma [Young et al., 1998] and H_2O/SO_2 ratios of 200-1000 [Woods et al., 2002]. Measurements of dome rock suggest permeability values in the range $K = 10^{-14}$ to 10^{-12} m^2, including the effects of pervasive fractures [Melnik and Sparks, 2002]. Gas is assumed to be steam with a temperature of 850° C and vapor viscosity 2×10^{-5} Pa s [Woods et al., 2002]. These results yield overpressures of the order 5-10 MPa throughout much of the dome for $K = 10^{-12}$ m^2, and higher values for lower permeability. For the range of permeabilities considered, the mass of solid fraction ranges from 12 to 25×10^9 kg, whereas the net mass of exsolved gas (water vapor) in the dome ranges from 3 to 15×10^6 kg. This is an important result that constrains the dynamics of the fragmenting mixture. Such pressurized domes have two to three orders of magnitude less exsolved volatiles per mass of magma than is present in a typical Plinian eruption, and this leads to a substantially greater density of the pyroclastic currents produced [Woods et al., 2002].

The particle size distribution of the Boxing Day blast deposit was estimated by Ritchie et al. [2002] using well-established sedimentological techniques, although much uncertainty remains in the characterization of pyroclastic mixtures, particularly when large portions of the flow are lost to sea. Based on these deposit studies and additional field work of our own, we use three particle sizes (5000 μm; 500 μm; 50 μm) to represent particle classes >2000 μm, ~125 μm, and <125 μm, respectively, yielding the bulk proportions 25, 40, 35 wt%. A density of 2300 kg m^{-3} is used for the largest particle size, otherwise particle density is 2600 kg m^{-3}. Although the three populations cannot cover the full spectrum of grain sizes in the deposits, particularly the coarse tail, our choice was dictated by both computational efficiency and the physical model (constitutive equations) which cannot treat clasts larger than several mm. Furthermore, the model does not treat changes in grain size due to aggregation and secondary fragmentation, processes which have yet to be quantitatively characterized. We refer the reader to previous work which explicitly explores the effects of grain size simplifications on 2D model results [Neri and Macedonio, 1996; Neri et al., 2003] and leave the corresponding 3D study for future work.

The volume of dome lava involved in the blast and its associated high-energy PDC was ~25 × 10^6 m^3 dense rock equivalent (DRE). This value is relatively well constrained, but because the total duration of strong activity was ~11.6 min and occurred in several pulses, we partitioned the total volume into smaller quantities representing individual pulses. Our main constraint is on the *total* volume of original dome, which limits the sum of individual pulse volumes, apart from additional materials entrained. For our models we therefore consider representative volumes of ~5 and 10 × 10^6 m^3 DRE, representing relatively small and large pulses, according to arguments outlined in Section 2.

4. 2D Simulation results

Before conducting the 3D simulations, we performed a number of 2D sensitivity runs using PDAC. Here we present three of these, illustrating the influence of solid mass (or volume), and gas energy (via the influence of permeability on dome pressurization), on flow evolution. The first comparison between simulations examines the influence of mass released by varying volume DRE (5 and 10 × 10^6 m^3), independently of permeability, which remains constant at $K = 10^{-12}$ m^2. The second comparison examines the effects of gas pressure and energy, by varying pre-blast dome permeability ($K = 10^{-12}$ m^2 and 10^{-14} m^2), while keeping volume constant at 5 × 10^6 m^3 (Table 1). The computational domain extends 10 km radially and 8 km vertically, with a non-uniform mesh resolution increasing very gradually, from 10 m close the left boundary axis of symmetry and above the topography, to 100m on the right edge and the top atmospheric boundaries. The non-uniform mesh allowed us to increase the resolution in the regions near the source and the ground, where we observe the largest gradients in the flow variables. The location of the topographic profile used in all 2D simulations is shown in Fig 2 (A-A') and includes the offshore sea surface. Although the dense basal portion of pyroclastic flows can travel underwater, pyroclastic surges on Montserrat have been observed gliding over the sea [Montserrat Volcano Observatory, unpublished data; Hart et al., 2004].

4.1 Large-scale features

Simulation A-2D uses a high permeability value of $K = 10^{-12}$ m^2 resulting in internal gas pressures from 10 MPa at the base of the dome to atmospheric at the surface The solids volume $V_{DRE} = 5 \times 10^6$ m^3 assumed for the ~70° sector corresponded to a mass per unit angle of $(5 \times 10^6/2\pi) \times (360/70)$ m^3/radiant for input in the cylindrical coordinate simulation. An estimate of the volatile energy stored in the dome is given by the specific work, and the range of values (see Table 1) correspond to purely adiabatic (lower limit) or purely isothermal (upper limit) expansions [Woods et al., 2002]: $E_s = 320\text{-}490$ J kg^{-1}. Simulation B-2D uses a greater dome volume of 2X that of A-2D ($V_{DRE} = 10 \times 10^6$ m^3 for the 70° sector; $E_s = 390\text{-}610$ J kg^{-1}), but is otherwise nearly identical to A-2D. The specific energy is slightly greater in B-2D due to the non-linearity of the pressure distribution within the dome. Simulation C-2D uses $K = 10^{-14}$ m^2, which results in greater interior pressures and much higher gas energy: $E_s = 1880\text{-}3380$ J kg^{-1}. The volume is identical to A-2D.

In simulation A-2D (Figure 3), an initial quasi-spherical expansion occurred, reaching maximum gas velocity of ~160 m s^{-1} at 0.2 s. Corresponding peak particle velocities varied with particle size; 75, 125, and 155 m s^{-1} for particle diameters of 5000, 500, and 50 μm, respectively. Lateral velocities were greater than vertical by 0.3 s. At 2 s, the vertical mixture speed was ~120 m s^{-1}, and horizontal speed was 170 m s^{-1}. We call this first stage the burst phase, in which the dynamics are primarily controlled by gas expansion and associated particle acceleration, and are strongly affected by the initial total specific gas energy. Velocities in the burst phase are generally higher than the sound speed of the pyroclast mixture, which is much lower than the atmospheric sound speed because of the relatively high particle concentration. Nevertheless, we propose that any leading atmospheric pressure wave was weak [$(p_{after}/p_{before}) < 1.5$] for three reasons; the initial velocities of the pyroclast mixture were much less than sound speed in atmosphere, ~330 m s^{-1} at standard ground conditions, the pressurized fluid was a solid-gas mixture with a low gas volume fraction, and the pressure ratio between the dome's interior and the atmosphere prior to blast initiation was less than 100 [Chojnicki et al., 2006].

The erupted material fails to mix with sufficient air to form a buoyant column and thus, at $t > 5$ s, collapses below the source, initiating the collapse phase (Fig. 3a). The material then moves parallel to the ground surface in the PDC phase beginning between 15 and 20 s after onset (Fig. 4). The transition from initial burst to PDC phase is highlighted by the trajectories of the fluid parcels from 0 to 15 s (Fig. 3b). The trajectories are characterized, in the first seconds, by ballistic paths, where the outermost portions of the dispersed dome pyroclasts reach the maximum height (>1300 m a.s.l., 250 m above the dome). We interpret the start of the collapse phase as the point in time when a preponderance of "ballistic" paths have passed peak height and are inclined downward and outward. The phases defined here are to some extent gradational.

The transformation to the PDC was mostly complete by 15-20 s, with the flow front ~1 km from source, and PDC velocity about 70 m s^{-1}. The evolution of the PDC is illustrated by the isocontours of the total particle volumetric fraction at selected times in Fig. 4. At 40 s the PDC head has reached a distance of about 2700 m from the source where particles start to be elutriated by vertical convection. Mixing of the PDC with the atmospheric air occurs mainly through the entrainment at the flow head, as evidenced by the thickened nose. At 90s the flow head has reached 5 km and has grown by air entrainment and expansion. A vertical convective plume is rising above the vent and small co-PDC clouds are developing where topographic slope abruptly changes and because of vortex instability in the tail. At 180s the elutriation of particles by co-PDC plumes is more developed, while the velocity of the PDC head is greatly reduced, and now consists of a dilute ash current overlying a dense basal flow. Nevertheless, it is worth recalling that the boundary condition at the bottom does not account for the interaction of the PDC with the sea surface or for the loss of particles by deposition so that the run-out of this thin basal flow could be overestimated, especially using a coarse mesh [Neri et al., 2003; Dartevelle et al., 2004; Appendix]. At 240 s the PDC head has stopped and an intense co-PDC plume develops at 6 km, while a dense basal flow has reached the distance of 10 km. The animation of the results better represents the temporal evolution of the burst and PDC propagation and can be seen on Movie S1 in the on-line auxiliary material.

In simulation A-2D, more than 95% of the total solid mass fed into the PDC. A small fraction (less than 5%) of the mass fed the plume above the dome (Fig 4 at 90s). Co-PDC plumes developed downslope after ~80 s, reflecting gravity segregation of fine versus coarse particles in the PDC, and development of mixture buoyancy by air entrainment; the plumes elutriated about 50% of 50 μm, 20% of 500 μm, and a negligible fraction of 5000 μm particles. The mass in the PDC was computed by integrating the particle bulk density in the sub-domain where $R > 1$ km and $Z < 0.9$ km, whereas elutriation by the co-PDC was calculated over the sub-domain where $Z > 0.9$ km.

Simulation B-2D begins with double the dome volume of A-2D, with parameters otherwise the same. B-2D produced the longest runout PDC of all 2D simulations due to its higher mass. Initial quasi-spherical expansion in the burst phase achieved peak gas velocities ~160 m s^{-1} at 0.2 s, but peak particle velocities varied with particle size. The burst phases of A-2D and B-2D are very similar, because the specific gas expansion energy is of the same order of magnitude (Table 1). At 2 s, vertical mixture speed was ~115 m s^{-1}, and horizontal speed was 200 m s^{-1} (Fig. 5a). The erupted material failed to become buoyant and at $t > 5$ s, and collapsed below the vent. The current then moved parallel to the ground surface in the PDC phase at t > 10 s, with the flow front ~1 km from source, and slope-parallel velocities of roughly 80 m s^{-1}. The trajectories of the fluid particles are similar to A-2D, with a very short expansion phase followed by the sudden collapse of the stream (Fig. 5b).

The temporal evolution of the B-2D PDC is similar to A-2D up to 90s (Fig. 6 and Movie S2 in auxiliary material), although the flow front moves faster due to higher inertia. The main differences can be observed after 130s when the flow head does not significantly slow down while the co-PDC plumes begin to develop in the flow tail. Instead, at 180s the PDC head structure is preserved without showing significant deceleration and has reached a distance of 10 km. The elutriation of particles occurs only in the PDC tail, so that it exerts a negligible effect.

Next we examine simulation C-2D, which begins with a dome volume identical to A-2D but K has been reduced to 10^{-14} m^2. The lower permeability results in greater interior pressures of several tens of MPa and much higher gas energy than A-2D. Because these magnitudes exceed previous estimates of conduit pressures [Clarke et al., 2002a,b; Voight et al., 1999], we consider this an extreme upper-bound case but useful to explore the effects of high dome overpressures on the blast. As a consequence of the higher gas energy (compared to A-2D) the initial quasi-spherical expansion reached a maximum gas velocity of 175 m s^{-1}, with corresponding peak particle velocities of 80, 145, and 175 m s^{-1} for particle diameters of 5000, 500, and 50 μm, respectively. At 2 s, vertical speed was ~140 m s^{-1} and horizontal speed was 188 m s^{-1}, and at 5 s, the average speeds were 106 m s^{-1} vertically, and 150 m s^{-1} horizontally (Fig.7a). The erupted material again failed to mix with sufficient air to form a buoyant column and thus, in the gravity collapse phase at t > 5 s, collapsed downslope in a stream of ash, blocks, and gas. The material then moved parallel to the ground surface in the PDC phase at t > 20 s (Fig. 9). The burst phase of C-2D is characterized by a violent radial expansion of the mixture, with fluid parcels following almost ballistic trajectories up to 10 s and greater than 500 m above the dome (Fig. 7b). Despite the high internal dome pressure, even in this case the atmospheric pressure perturbation rapidly decays with distance from source. Perturbations of the atmospheric pressure in the first 10 s at different distances from the dome are shown in Figure 8. Values are sampled at 5 m above the ground. The plots clearly identify the arrival of the pressure wave caused by the burst. The overpressure is about 15 kPa at 1 km, creating a weak pressure wave of strength (p_{after}/p_{before}) < 1.2, and decreases to only a few kPa at 3.5 km. Overpressures >2 kPa are sufficient to cause tree blowdown [Valentine, 1998a], although the interior dome pressures assumed for C-2D are extreme.

The transition from collapse phase to PDC phase occurs at ~15-20 s. PDC front speeds are ~90 m s^{-1} at the transition. The temporal evolution of the PDC (Fig. 9, Movie S3 in auxiliary material) is similar to A-2D except that co-PDC plume development is more vigorous due to the greater initial expansion of the mixture associated with higher dome pressure. An intensely buoyant co-PDC plume develops from the flow head at a distance of 5 km at about 150 s and is then pulled vent-ward by the strong vertical convection above the vent (Figure 9, 180 s). At 240s the co-PDC plume extends to about 4 km from the source while a dense, thin basal flow has reached the distance of 10 km. The co-PDC plumes elutriated about 65% of 50 μm, 30% of 500 μm and <5% 5000 μm particles.

4.2. PDC dynamics

Figure 10 shows the PDC front positions vs. time and the PDC front velocity vs. distance from the source. The front is tracked by measuring the most advanced part of the PDC, without distinguishing between the flow head and the thin basal layer. The "low energy" blasts (A-2D and B-2D) display nearly parallel trends, with B-2D's flow velocity systematically higher than that of A-2D. The slight change in slope of the A-2D distance-time curve occurs where the current becomes positively buoyant and decelerates as a result. The more energetic blast (C-2D), on the contrary, attains the highest initial PDC velocity of all three 2D simulations (Fig. 10b) but decelerates rapidly due to extensive entrainment of atmospheric air and subsequent development of positive buoyancy in portions of the flow. As a result, the final PDC run-out is comparable with that of A-2D.

The trends of the front velocity vs. distance (Fig. 10b) are very similar for A-2D and B-2D even though the former shows more pronounced changes in the front velocity at 4 km (corresponding to the break-in-slope) and 6 km (where the co-PDC plume forms). On the other hand, the PDC front of C-2D developed a very high lateral velocity in the burst phase (please note that the front velocity does not necessarily coincide with the maximum flow velocity) while it decreased more rapidly corresponding to breaks-in-slope and subsequent entrainment.

Figure 11 compares mixture density, mixture velocity, and dynamic pressures, as a function of time, at 10 m above the ground surface at sampling positions 2, 3, and 4 km from the source. The left plots refer to simulations with lower dome volume (A-2D and C-2D), whereas the right plots refer to the higher volume (B-2D). The dynamic pressure is computed from the mixture density $\rho_m = \varepsilon_g \frac{P\bar{\mu}}{RT_g} + \sum_s \varepsilon_s \rho_s$ and the horizontal and vertical mixture velocity components $(u_m, v_m) = \frac{1}{\rho_m}\left[\varepsilon_g \frac{P\bar{\mu}}{RT_g}(u_g, v_g) + \sum_s \varepsilon_s \rho_s (u_s, v_s)\right]$, according to $P_d = \frac{1}{2}\rho_m \sqrt{(u_m{}^2 + v_m{}^2)}$. In the preceding equations, $\bar{\mu}$ is the averaged molecular weight of the gas mixture, P and T_g are the gas pressure and temperature, R is the universal gas constant, ρ_s is the density of the pyroclasts, ε is the volumetric fraction of a phase and the subscripts g and s refer to the gas and solids, respectively.

Mixture density plots (Fig. 11) show a peak corresponding with the passage of the flow head. This peak decreases in magnitude with distance from source, which we interpret to indicate flow head dilution. However, at later times (e.g., 100 s), the PDC mean density is controlled by the competing effects of intra-current sedimentation of particles and elutriation via a buoyant gas stream. For A-2D, peak densities of ~57, 19, and 18 kg m^{-3} occurred at the three sampling positions at times ~50, 70, and 100 s. For C-2D, very similar values are reached about 10 s earlier. In contrast, B-2D produced peak densities of ~118, 38, and 30 kg m^{-3} at the same locations, roughly double the values of the other two runs. Nevertheless, it is worth noting that the exact values of the density in the basal cells can be affected significantly by the mesh resolution. The sedimentation process is influenced by the vertical mesh size and deposition, as discussed above, and deposition is not explicitly treated by the model. The sensitivity of model results to grid resolution is discussed in detail in the appendix.

Mixture velocity also decreases with the distance from the vent and after the passage of the flow head. Please notice that mixture velocity 10 m above the ground is generally much lower than the front velocity (compare Fig. 11 to Fig. 10b), due to flow stratification. For A-2D, maximum velocities of 46, 40, and 34 m s^{-1} occurred at 2, 3, and 4 km at times ~35, 60, and 75 s, respectively. For C-2D, maximum velocities at 2, 3, and 4 km, 10 m above ground, are 72, 44, and 33 m s^{-1}, at 23, 50, and 60 s, respectively. Apart from higher speed at the 2 km position, the values are close to those of A-2D, but occur 10-15 s earlier. For B-2D, peak velocities were 66, 43, 40 m s^{-1}, at times of 26, 50, and 65 s. Peaks in velocity always occur earlier than peaks in density, indicating that the arrival of the dilute ash cloud precedes the arrival of the dense basal layer. The large oscillations after about 110 s reflect the development of convective co-PDC plumes.

For A-2D, dynamic pressure peaks of ~44, 13, and 7 kPa occurred at the sampling positions at times of ~45, 65, and 90 s, about 15-20 s after the arrival of the PDC front. Similar values for C-2D occur almost 10 s earlier, because of the larger initial velocity of the burst phase. For B-2D, dynamic pressure peaks of ~75, 28, and 14 kPa, occurred at the sampling positions at times ~48, 65, and 80 s, about 20 s after the arrival of the PDC front. The A-2D and C-2D simulated peak dynamic pressure in the region of severe damage at St. Patricks and Morris (at about 3.4 km from the source) were between 10 and 15 kPa, values less than those estimated to explain the damage observed [Sparks et al., 2002; Baxter et al., 2005]. On the contrary, for B-2D, simulated dynamic pressure in the same region was as much as 25 kPa, consistent with the minimum value (>25 kPa) proposed by Sparks et al. [2002] and Baxter et al. [2005] to explain the damage observed. The reader is cautioned that these near-ground (~10 m) dynamic pressures could be significantly underestimated due to a grid size effect (see Appendix, Fig. A2). Nevertheless, the general conclusion appears to be sustained.

An interesting feature of these simulations is that velocities in the region of severe damage between 3 and 4 km appear to be similar for A-2D, C-2D and B-2D, i.e. 33-43 m s^{-1}, whereas doubling the mass approximately doubled the peak mixture density, and doubled the dynamic pressure. We therefore conclude that damage potential on Montserrat may be linked more closely with high mixture densities than with unusually high current speeds.

Modeled mixture temperatures were also recorded at 2, 3, and 4 km positions, 10 m above ground. For all runs, and in all cases, peak values are roughly ~800°C, close to the initial temperature of the lava dome**.** These high peak values indicate that the basal layer of the PDC can keep high temperatures despite the intense air entrainment in the overlaying ash cloud. At 90 s convective plumes increase entrainment and plume temperatures drop to 200-400°C. Erosion and entrainment of cold substrate material on Montserrat undoubtedly contributed to temperature reduction, but are not treated in these simulations. Nevertheless, high temperatures of the ash in the Boxing Day event caused rapid ignition of furniture and combustibles, and was a major source of damage even at the periphery of the impacted area [Baxter et al., 2005].

Fig. 12 shows the dynamic pressure at R = 3.4 km (the distance relevant for damage observed at St. Patricks) at 10 m above ground. For A-2D, the onset of the jump in dynamic pressure associated with the arrival of the PDC front at SPT seismic station (at R = ~3.4 km) occurred at ~60 s, whereas the peak dynamic pressure occurred at ~70 s. For B-2D the flow front arrived at ~50 s with a peak at ~70 s. For C-2D the flow front arrival and peak dynamic pressure roughly coincide at ~50-55 s. Given that the initial dome radius is 230 m, the average velocity for A-2D was (3400-230 m)/60 s = 53 m s^{-1}, whereas for B-2D and C-2D, the velocity was approximately 63 m s^{-1}. These values are close to the average velocities of 38-56 m s^{-1} inferred from the timing of the first seismic pulse, but <50% of the velocity inferred from the second seismic pulse (113 m s^{-1}). Our models therefore support the hypothesis that the first pulse destroyed the station, although we must emphasize that average velocities fail to capture the complex velocity vs. distance estimates discussed in previous sections. The main 2D simulation results are summarized in Table 2.

5. 3D simulation results

Guided by the 2D parametric runs, the 3D PDAC code was applied over a Digital Elevation Model (DEM) with a 20-m grid. The DEM represents conditions just before the blast, with topography from a debris avalanche deposit filling much of the original White River valley. The 3D computational domain is extended 9 km in longitude (from X=76160 to X=85060 on the UTM map), 9 km in latitude (from Y=41560 to Y=50460) and 6 km vertically. The horizontal mesh resolution varies, very gradually, from 20 m near the source up to 200 m on the lateral boundaries. The vertical resolution varies from 20 m over the first 800 m, and gradually increases to 200 m at the top of the domain. The non-uniform mesh allowed us to increase the resolution in the regions near the source and the ground, where we observe the largest gradients in the flow variables. The initial dome is represented by a hemisphere centered at coordinates [X=80690m; Y=46550m; Z=710m] on the summit flank, sloping to the south [see topography Figure 13]. Two 3D simulations are presented here, A-3D ($V_{DRE} = 5 \times 10^6$ m^3), and B-3D ($V_{DRE} = 11 \times 10^6$ m^3). For both cases, $K=10^{-12}$ m^2. We compared the simulation results against one another, and against maps of deposits and destruction and observational data [Sparks et al., 2002; Ritchie et al., 2002; Baxter et al., 2005].

5.1. Large-scale features

The results of the 3D runs are shown in Figure 13 and 14. Fig. 13 (vertical slice through the dome center, parallel to PDC propagation direction) shows the initial *burst* phase for simulations A-3D (a) and B-3D (b). The simulation is characterized, as in the 2D cases, by an initial expansion phase at t < 5s, when the pyroclastic mixture expands into the atmosphere forming a quasi-spherical shell. The subsequent collapse of the cloud at t ~10 s produces a PDC which travels down slope. The asymmetry of the collapse is due, in 3D, to the source topography that provides an initial tilted flank on which the source rests, and an impediment to the propagation toward the Northern sector. The blast phase is very similar for A-3D and B-3D since the initial specific energy is nearly identical (Table 1).

Fig. 14a shows simulations A-3D propagating over a 20-m DEM of southern Montserrat viewed to the north. The evolution of the blast and blast-generated PDC is illustrated by color contours that represent total volume particle fraction, decreasing from dark (10^{-2}) to light (10^{-6}). The figure illustrates important effects associated with local topography, including accelerations affected by steep slopes, non-radial motions caused by obliquely-orientated topographic elements, particle-size segregation better developed in channels than on interfluves, and topography-influenced formation of buoyant plumes near the source and above the PDCs. At 10 s (not shown) early gravitational collapse feeds the PDC, followed by topographic segregation into two distinct PDC lobes. By 30 s the PDC is spreading over a broad sector of the landscape, with its main axis directed through St Patricks village, and segregation into local channels is shown by the development of several lobes. There is a weak rise of near-source buoyant plumes. Just after 60 s only one lobe exists, in the White River valley. By 90 s, multiple buoyant plumes are evolving above the source region, while the densest portion of the main lobe verges on St Patricks village, and the more dilute front extends over a 70° sector and to nearly 2 km offshore.

The second 3D simulation, B-3D (Fig. 14b), is representative of the higher-volume destructional/erosional pulses. The PDC flow features are generally similar to, but more strongly developed than, the previous run of Fig. 14a. At 10 s (not shown), early gravitational collapse feeds the PDC, followed by topographic segregation. By 30 seconds the PDC has spread over a 60° sector, centered about a main axis aligned to the southwest. Two lobes have developed, concentrating most of the mass in the White River channel; the current also moves in places over interfluves, aided in some cases by runup at channel bends. The densest portions of the two lobes remain beyond 60 s. By 90 s, the densest portion of the PDC occurs as a single lobe, and the PDC front has bypassed St Patricks and extends 3 km offshore, while multiple co-PDC plumes are rising above the source region.

Further details of the 3D simulations are illustrated by contours log of the particle volume fraction 10 m above the topographic surface and along a longitudinal (LL') and a transverse (PP') section (Figure 15). The particle maps (Fig. 15a,d) show, in both cases, a channelized flow to the east, in Dry Ghaut, recognized also in the field [Fig. 2; Druitt et al., 2002]. The model blast-affected sector is roughly 70° in both simulations and compares well with the mapped distribution (Fig. 2 and bold line in Fig. 15a,d). In both A-3D and B-3D, particles concentrate near the base of the flow whereas co-PDC plumes generally develop at slope breaks and are significantly more dilute (Fig. 15b,c,e,f). The highest particle concentration occurs in channels and decreases with height above the surface (Fig. 15b,c,e,f), and laterally away from the centerline of the deepest channels (Figs. 15c,e). In general, current velocities are greater in the 3D simulations due to channeling effects, but some general trends are similar to the 2D runs. For example, doubling the dome mass (Simulation B-3D) also increases the PDC density, dynamic pressure and velocity, and decreases the elutriation rate (as in 2D).

Field studies of the SHV deposits provide evidence that mobile dense basal flows drained into channels which did not directly connect with the primary source area (secondary flows), including ravines west of St Patricks and Dry Ghaut to the east of the vent. They were immediately recognized as representing an important, but puzzling and hitherto underestimated hazard around active lava domes [Druitt et al., 2002]. The 3D simulations presented here strongly suggest that this type of hazardous flow can form in blast-type eruptions by PDCs which cross interfluves. Particle velocity vector maps (Fig. 16) augment the maps of particle distributions and compare well to blowdown features in the blast-affected area [Sparks et al., 2002; Baxter et al., 2005], as well as illustrate development of these secondary flows (originating near the summit, flowing to the East in Dry Ghaut). On the other hand, simulation B-3D produced a northward directed PDC lobe, which was able to overtop the summit. This type of PDC was not observed in the natural event, and we attribute the inconsistency mainly to the weak constraint to northerly motion provided by the modeled source topography. Animated results from three oblique views of both 3D models runs display the dynamic evolution of the phenomena mentioned above, and can be viewed on on-line auxiliary material (Movies S4 to S6).

In both 3D models (map not shown) high temperatures in the basal part of the currents extended even to the periphery of the PDC, where dynamic pressures were low. This is consistent with field observations that temperatures were high and rapid ignition was a primary source of building damage along the periphery of the affected zone [Baxter et al., 2005].

5.2 PDC dynamics

The dynamic pressure, mixture density and mixture velocity at fixed probe locations (shown by dots in Fig. 16) through time show that the dynamic pressure decreases with total mass erupted as in 2D (Fig. 17). For example, consider the dynamic pressure along the flow axis for the two runs at 2.2 km from source (Fig. 17, top two panels, solid lines). Doubling the dome mass more than doubles the dynamic pressure, which can be attributed largely to an increase in PDC density (Fig. 17, middle two panels), and, to a much lesser degree, to changes in PDC velocity (Fig. 17, bottom two panels). This comparison agrees with the 2D calculations which suggest that the dynamic pressure is roughly proportional to the erupted mass and increases largely due to an increase in flow density, rather than to an increase in flow velocity. Dynamic pressure also decreases significantly with distance from source and with distance from the PDC axis towards the flow periphery, again with changes in flow density causing the bulk of the changes in P_{dyn} (Fig. 17). For instance, the dynamic pressure of A-3D at 2.2 km from source along the flow axis is nearly six times the dynamic pressure along the flow periphery at the same distance from source, and is roughly three times the dynamic pressure along the flow axis at 3.2 km (Fig. 17, top left panel).

The maximum dynamic pressure recorded at 10 m above the ground, 90 s into simulation A-3D, is mapped in Fig. 18a. The map further illustrates that maximum dynamic pressure decreases steeply with distance from source and with distance from the main and secondary flow axes. The longitudinal (Fig. 18b) and transverse (Fig. 18c) sections show the steep decay in more detail. The maximum dynamic pressure calculated by A-3D near St. Patricks is about ~7 kPa, compared to estimates of >25 kPa required for the complete destruction at this axial locality [Sparks et al., 2002; Baxter et al., 2005]. And, for A-3D, peripheral areas experienced slowly-building peak pressures <5 kPa. Therefore, simulation A-3D suggests that dynamic pressures resulting from a collapse of ≤ 5 million cubic meters are probably too small to explain the most severe damage observed. Although these simulated near-ground dynamic pressures could be underestimated by a factor of about two because of the grid size effect (Appendix, Fig. A2), the general conclusion appears to be robust.

The maximum dynamic pressure achieved by B-3D near St. Patricks is about 16 kPa (Fig. 18d,e,f). This value underestimates the actual dynamic pressure by a factor of about two because of the grid size effect (Fig. A2), so we conclude that this result is roughly consistent with estimates of >25 kPa based on field observations [Sparks et al., 2002; Baxter et al., 2005]. The much lower dynamic pressures in peripheral areas are also consistent with field-based estimates from damage. Therefore the dynamic pressures calculated for the B-3D case can account for the destruction observed both along the main axis and peripheral areas.

A further aspect of dynamic pressure is related to the ability of a PDC to pick up and entrain large rocks, trees, concrete slabs, etc., with these “missiles” themselves having the capability to cause severe damage [Esposti Ongaro et al., 2002; Sparks et al., 2002; Baxter et al., 2005]. Following the analysis by Wills et al. [2002], dealing with missiles transported by heavy winds, in a steadily increasing current the condition for flight of a loose object is,

$$P_d\, C_D > \rho_s\, L\, g,$$

Where P_d is dynamic pressure, C_D is the drag coefficient, ρ_s is density of the object, L is the characteristic dimension of the object, and g is gravitational acceleration. The maximum size of the object is thus proportional to the dynamic pressure and inversely proportional to density of the object.

Applying this relation to the PDC dynamics at St. Patricks, we calculate maximum size L of a loose lava block borne by the PDC. Assuming C_D is approximately one for a bluff body, P_d = 25 kPa, and ρ_s = 2000 kg m^{-3}, yields a maximum block dimension L = 1.3 m, which is consistent with the meter-sized blocks observed embedded in heavily impacted houses on Montserrat [Sparks et al., 2002, Fig. 16c].

Damage due to such objects can be related to their kinetic energy K, given by

$$K = ½\, \rho_s V\, (\vartheta u)^2,$$

where V = volume, ϑ = fraction of the current speed attained by an object before impact, u = current speed. Assuming $V = L^3 = (1.3\ \text{m})^3 = 2.2\ \text{m}^3$, $\vartheta = 0.36$ (based on wind-tunnel tests for cubes [Wills et al., 2002]), and u = 45 m s^{-1} (sampled at 10 m above ground, Fig. 16), the kinetic energy is about 580,000 J. Since kinetic energies of a few tens of J are sufficient to seriously damage building components [Minor, 1994], such missiles can be considered an important hazard process related to PDC dynamics on Montserrat and elsewhere.

We finally note that dynamic pressures calculated for the 3D simulations represent a lower bound for the given volumes, because not all energy was focused directly to the south. For example, if the source boundary were changed to a quarter-sphere (with the same total volume as the hemisphere), with an east-west trending vertical back-boundary, the burst phase would be directed entirely to the south and would likely have been more damaging. We will explore the specific effects of source geometry in a future study.

6. Discussion

In general terms, the modeling results presented here have led to several scientific insights about the sudden decompression and subsequent destruction of a lava dome. According to our model results, the directed volcanic blast can reasonably be described by three main phases; the *burst*, *collapse* and *PDC* phases. It appears that dome permeability and source pressure distribution can influence blast characteristics, mostly affecting the burst phase and co-PDC plume development, and asserting lesser influence on asymmetric collapse characteristics and PDC velocity, density, dynamic pressure, and runout distance. On the other hand, total dome mass appears to exert the greatest control on PDC runout and dynamic pressure, which largely determine whether or not an event will be highly destructive. Comparison between 2D and 3D results indicates that topography strongly influences the dynamics of the PDC. For example the 3D results capture the evolution of enigmatic high-concentration mobile dense basal flows in several channels not directly connected with the primary source area [Druitt et al., 2002] and simulate the steep decline in dynamic pressure with lateral distance from PDC axes. From these comparisons, we conclude that 3D modeling with topography is essential for full analysis of directed volcanic blasts, especially for exploring the effects of channeling on the distribution of pyroclastic deposits.

Given that the observed damage and deposit characteristics are the primary evidence of the Boxing Day blast characteristics and dynamics, we made broad comparisons between model results and estimates made from field analysis. From these comparisons, we suggest several conclusions specific to the 1997 Boxing Day event at SHV. The 3D simulations generally capture the geometry of the mapped sector of the Boxing Day event, as well as numerous other basic characteristics of the distribution of the eruptive products, including the development of multiple PDC lobes with the highest concentrations occurring along channel axes, and the formation of secondary pyroclastic flows in lateral channels. High-volume simulations (in both 2D and 3D) calculate PDC dynamic pressures consistent with field observations of structural damage, while dynamic pressures associated with low-volume simulations appeared insufficient to explain observations, providing evidence that the observed severe damage was likely caused by high-volume pulses, rather than low-volume pulses. A systematic decrease in peak PDC dynamic pressure with distance from source and from lobe axes was also reproduced, in accordance with the observed damage. Modeled temperatures are high over the extended region of the PDC even at the periphery where dynamic pressures were low, consistent with ignition being the major source of observed damage in those areas [Baxter et al., 2005]. The relatively sharp rise in dynamic pressure at St Patricks (R = ~3.4 km; t = ~50 s) suggests average 2D model speeds of 53-63 m s^{-1}. These average speeds are reasonably consistent with estimates of 38-56 m s^{-1} inferred by assuming that the first seismic pulse destroyed seismic station MSPT, but are roughly half of the velocity estimated by assuming that the second seismic pulse destroyed the station, supporting the hypothesis that the first pulse destroyed the station. These comparisons suggest that the model presented here, along with its simplifying assumptions, captured the essence of the large-scale dynamics of the lateral blast at SHV, and could be useful for understanding hazards associated with blasts in general.

For the 1980 Mount St Helens blast, Kieffer [1981, 1984] developed the hypothesis that the most severe zone of damage could be explained by supersonic flow (Mach number >3) within a shock wave-constrained flow field. Kieffer also proposed that the boundary between the 'direct blast zone' and the 'channelized blast zone' north of the vent corresponded to a transition from supersonic to subsonic flow marked by a Mach disk shock at ~11 km from source. Wohletz [1998], for the MSH blast specifically, calculated leading shock wave overpressures of 40 kPa and dynamic pressures of 1 kPa at 10 km using the full thermal energy (7 Mt) released during lateral propagation of the blast, and assuming that the energy release time and empirical relations were similar to surges driven by a surface nuclear explosion [Glasstone and Dolan, 1977]. We discuss supersonic flow and shock waves below within the context of the Boxing Day event on Montserrat.

Under the assumption of mechanical equilibrium between the phases, no heat transfer between them, and no compressibility effects in the solid phases, the sound speed in a multiphase gas-particle mixture can be computed by the formula:

$$c = \left(\frac{\gamma_g R T_g}{Y} \right)^{\frac{1}{2}} \left(Y + (1-Y) \frac{\rho_g}{\rho_s} \right)$$

where Y is the mass fraction of gas in the multiphase mixture, ρ_g and ρ_s are the gas and solid densities, T_g is the gas temperature, γ_g is the ratio of specific heats for the gas phase, and R is the perfect gas constant [Wallis, 1969; Dobran et al., 1993, Gidaspow, 1994]. Depending on the transformation, γ_g can be equal to 1.4 (adiabatic expansion of gas) or 1 (isothermal expansion). Due to the multiparticle nature of the mixture and therefore to the different degrees of equilibrium between gas and particles we tested both adiabatic and isothermal conditions. Nevertheless, the large exchange area between gas and particles, together with the high concentration of solids at the base of the PDC, favor (as shown by simulation results) an isothermal expansion. Therefore we prefer the value $\gamma_g = 1$. Moreover, as a first-order estimate, we did not include a slip velocity correction due to its relatively small value compared to the horizontal flow speed. The above equation has been validated by Gidaspow and Driscoll [2007] by showing it appropriately describes the propagation of pressure waves through a fluidized bed over a wide range of void fractions. According to it, the sound speed of the mixture decreases with increasing particle volume fraction until a minimum is reached at a void fraction of 0.5. Similar estimates of the sound speed of the eruptive mixture can be obtained by using the pseudogas approximation; for instance Kieffer [1981] assumed γ_{mix} = 1.04 and obtains soundspeed values within a difference of few percent of our values. The associated Mach number is defined as $M = \frac{\sqrt{u_m^2 + v_m^2}}{c}$, where u_m and v_m are the mixture horizontal and vertical velocity components, respectively. Because the sound speed can be quite low in our gas-particle mixtures, we now explore the Mach numbers in C-2D and B-2D, the simulations most likely to exhibit supersonic flow. Simulation C-2D has the highest burst velocities, whereas B-2D exhibits the highest PDC velocities and has the lowest mixture sound speeds due to high particle concentration. Figures 19 shows Mach number contours for these two simulations.

For B-2D, the transformation from the burst phase to collapsing stream occurs in the first few seconds and the transformation from collapse phase to PDC phase is largely complete by 10 s (Fig. 19a). The PDC displays a local supersonic basal region, enhanced by topography. For instance at 30 s (Fig. 19b), isolated regions with M > 1.6 occur in front of local steep areas that promoted acceleration. By 50 s (Fig. 19c), M > 1 occurs in a thin basal zone limited to 1.6 - 2.3 km from source, whereas the PDC has spread to 3.6 km, and dynamic pressures >15 kPa (and rising) already occur in the subsonic region at 3 km (see Fig. 11 above).

C-2D shows the development of a concentric region of supersonic flow at 1 s in the burst phase (not shown), grading to a broader and gradually less concentric region of supersonic flow (with M >2) in the laterally-directed collapsing stream (Fig. 19d at 10s). By 30 s the flow is subsonic nearly everywhere, except a very narrow region (R~1 km) where M >1 in the PDC body (Fig. 19e). At later stages the flow Mach number decreases due to deceleration. At 50s (Fig. 19f) the maximum Mach number is roughly 0.8 at 3-4 km from the source.

The distribution of the mixture Mach number (over the dispersal sector at 10 m above the ground) is shown for simulation B-3D at 50s (Figure 20). The mixture sound speed is computed from the same relation used above, and ranges from 40 m s^{-1} at the base of the PDC (where the particle concentration is the highest) to about 400 m s^{-1} in the dilute ash-cloud, where the ash concentration is low but the temperature is still high. Maximum Mach number of approximately 1.0 occurs in a small patch along the main channel, where the velocity and the flow density are the highest, but apart from this the PDC is internally subsonic. Along longitudinal (Fig. 20b) and transverse sections (Fig. 20c), the distribution of the Mach number is very similar to that observed in 2D, with the highest values occurring in the basal layer of the PDC. The Mach numbers in run A-3D (not shown) are everywhere subsonic, suggesting that in the simulated events, supersonic effects are of very local occurrence and of minor importance. To summarize, our model results suggest that the flow is only locally supersonic (in correspondence with the regions with high particle concentrations) and strongly transient, so that we can reasonably exclude any important effect due to strong, persistent internal shock waves, beyond the burst phase and region (up to 2 s after onset and distances < 1 km).

For the 1980 Mount St. Helens blast, it was hypothesized that an overpressured jet horizontally emanated from a vent, resulting in a strong (Mach disc) shock normal to the blast direction [Kieffer, 1981]. In such an underexpanded jet, the flow accelerates due to the decompression and is supersonic in an extended region between the vent and the shock. Based on our Montserrat simulations, we cannot exclude the possibility that increasing the scale (total mass and energy) of the eruption to the size of the MSH blast could lead to the formation of a short-lived overpressured jet. Nevertheless, according to the simulations presented here, the strongly transient behavior of a blast and the generally low Mach numbers in the corresponding PDC make us skeptical that a supersonic, underexpanded quasi-steady horizontal jet of wide extent existed during the Boxing Day event.

The severe damage at St. Patricks appears to have been caused by the high dynamic pressure of subsonic PDCs (>25 kPa), and impacts of large missiles (also related to dynamic pressure), rather than by shock waves associated with supersonic flow, given that calculated Mach number never exceeds unity in the region of damage. The existence of local regions of M >1 implies that perturbations of the flow pressure (e.g., due to sudden changes in the topographic profile) can generate internal shock waves. Nevertheless, no discontinuities were calculated in these model runs at the mesh scale (a recent application of the PDAC code to the simulation of the shock wave propagation in supersonic volcanic jets [Esposti Ongaro et al., 2006] has demonstrated that the code is able to accurately capture the flow discontinuities in the compressible regimes even using a relatively coarse mesh of more than 10 m). This conclusion, however, does not exclude the possibility of localized generation of internal shock waves in isolated regions, or of damage by supersonic flow in the very proximal area. We also note that with some alternative source conditions, the burst phase could be more focused to the south.

7. Conclusions

Based on our model simulations we are able to separate the transient directed-blast at SHV into three main parts, the *burst phase*, the *collapse phase*, and the *PDC phase*. In the burst phase, the pressurized mixture is driven by kinetic energy of the gas phase, expanding rapidly into the atmosphere, with much of the expansion having an initial lateral component because of the geometry of the pressure release surface. The erupted material fails to mix with sufficient air to form a buoyant column and thus, in the collapse phase, falls beyond the source as a stream of gas and pyroclasts. The material then moves parallel to the ground surface as a density current in the mainly subsonic PDC phase. Local supersonic flow is possible in the PDC phase, but it likely results from high mixture density, rather than extremely high velocities. This idealization of directed blasts contrasts with some previous models (Kieffer, 1981, 1984; Wohletz, 1998].

Our modeling results also indicate that the total mass in the PDC has great control on inertia and runout, and can largely determine whether or not an event will be highly destructive. Further, source permeability and source pressure distribution can strongly influence burst-phase characteristics and co-PDC plume development, but affects only minor control over asymmetric fountain characteristics and PDC propagation. Topography strongly influences the dynamics of PDC evolution, and only 3D models incorporating 3D topography can capture the effects of channeling on the distribution of PDC deposits. Despite the complexity of the phenomena, our simulation results were consistent with field observations of depositional features, structural damage, and damage due to fires ignited by the pyroclastic event. In particular our calculations suggest that the severe damage observed in the St Patricks area on Montserrat can reasonably be explained by high dynamic pressures and missile impact loading within subsonic PDCs generated by high-volume pulses.

Appendix

Numerical resolution on rectilinear meshes

The PDAC code solves the multiphase transport equations on a rectilinear mesh in 2D (cylindrical or Cartesian) and 3D (Cartesian) [Esposti Ongaro et al., 2007; Neri et al., 2007]. The discretization schemes adopted in the PDAC code are accurate to the second order in a Taylor expansion on a uniform mesh. In the simulations performed we adopted non-uniform meshes in order to reduce the number of cells and, consequently, the execution time of each run. The use of a non-uniform mesh allowed us to increase the resolution in the regions near the source and the ground, i.e. in the regions where we observe the largest gradients in the flow variables. In 2D, the computational domain extended 10 km horizontally and 8 km vertically and was discretized into 400×200 computational elements. The horizontal mesh size was uniform in the first 600 m with a resolution of 20 m, then increased radially up to 100 m at 6 km and then was left constant at 100 m up to 10 km. Vertically, the mesh size was uniform in the first 1500 m with a resolution of 10 m, then was increased gradually up to 60 m. In 3D, the computational domain was extended over a 9 km × 9 km area and up to 6 km vertically and was discretized into 128×128×100 cells. In this case, we adopted a horizontal resolution of 20 m, in a box of 500 m enclosing the source, and increased this gradually to 100 m beyond the 500-m boundaries. The vertical mesh resolution was uniform at 20 m for the first 800 m, and then increased up to 200 m. To reduce the numerical error, in both 2D and 3D, we limited the radial cell-size increase rate to 1.05, as is the common practice in numerical modeling. The numerical error strongly depends on the diffusion properties of the numerical scheme adopted and also on the flow Reynolds number. We therefore performed several sensitivity tests to evaluate the effects of the horizontal mesh non-uniformity and vertical mesh resolution on the numerical solutions.

Figure A1 presents the isocontours from -8 to -1 of the $\log_{10}$ of the total particle volumetric fraction in the atmosphere at 90 and 180 s for simulation A-2D and for various computational meshes, both uniform and non-uniform. The results show a minor effect of the mesh features on the large-scale dynamics of the PDC propagation. In particular, the effect of the horizontal cell stretching is negligible at 90 s (Figure A1, a and b), when the flow is almost entirely in the uniform region of the computational domain. At 180 s (Figure A1, e and f) some difference in the PDC runout can be observed, due to the different horizontal resolution (20 m vs. 100 m). The effect of the vertical resolution on the large-scale propagation of PDCs is also quite limited, as demonstrated by comparing the runout of PDCs at 90 s with a mesh of 6, 10, and 20 m (Figure A1, c, b, and d). At 180 s the difference is slightly more pronounced but still within a 10% tolerance. Similar results were obtained and discussed by Dobran et al. [1993] and Neri et al. [2003]. Similarly, in 3D, the comparison between maps of the total particle volumetric concentration at 90 s obtained with a uniform (50 m) and non-uniform (20-100 m) horizontal discretization (not shown) confirms the relatively minor effect of cell stretching on the solutions of explosion dynamics.

Because PDCs show strong vertical density and velocity gradients close to the ground, the influence of the vertical mesh resolution on dynamic pressure is more significant at the base of the flow. As a consequence, flow sedimentation and stratification computed by the model significantly depends on grid size, as already noted in multiparticle simulations by Neri et al. [2003]. For example, Figure A2 shows the influence of mesh size on vertical profiles of mixture density, velocity, and dynamic pressure for the PDC of simulation A-2D. From the plots one can see that the solutions begin to converge on a single solution as vertical grid size decreases (compare the change from the 20 m to 10 m grid to the change from the 10 m to 6 m grid). Generally speaking the smallest grid spacing, in this case 6 m, produces the most accurate solution. Results obtained with the 6 and 10 m meshes produce similar solutions and flow gradients. In detail, they produce similar velocity profiles with maxima about 50-60 m above the ground (Fig. A2, b and e), and nearly identical density profiles (Fig. A2, a and d). The resulting peak in dynamic pressure is approximately 20-30 m above the ground (Fig. A2 c and f). The similarity between the solutions on the 6 m and 10 m grids suggests that a resolution of 10 m is adequate to quantitatively describe the primary flow features. On the other hand, the solutions on the 20 m mesh significantly underestimate the maximum value of dynamic pressure (relative to the 6 m grid) and do not capture patterns close to the ground. Unfortunately, a 10 m mesh resolution is difficult to achieve in 3D simulations, because of the substantial increase in the total number of computational elements and associated computing time, and therefore a 20 m minimum grid size was adopted in our main 3D simulations. This choice does not significantly affect the large-scale dynamics of the explosion and PDC propagation (see Figure A1 above and similar analyses reported in Neri et al., 2003), but likely underestimates the PDC dynamic pressure by roughly a factor of two (Fig. A2c,f). Our results show that the dynamic pressure profile of the PDC is characterized, at least under the conditions considered in our simulations, by a sharp gradient from the ground to its maximum value at approximately 20-30 m above the surface. As a consequence, the estimate of dynamic pressure at 10 m above ground or lower may be subject to considerable uncertainty, due to the grid size effect and also the complex effect of the ground boundary condition on the flow behavior [Dufek and Bergantz, 2007].

Finally, it should be noted that mesh resolution also affects the accuracy of the topographic description. To reduce errors associated with inaccurate descriptions of topography we adopted a new immersed-boundary technique [De' Michieli Vitturi et al., 2007] suited to compressible multiphase flows in order to accurately describe, even with the relatively coarse mesh adopted, the no-slip condition at the interface between the fluid and the irregular 2D and 3D topography.

The computational grids used to date included up to 300 thousand cells in 2D and 2.5 million cells in 3D and required the challenging solution of several billions of algebraic equations. The parallelization strategy that allowed such an accomplishment was based on the decomposition of the domain among the computational processors by adapting the numerical solution algorithm to the parallel environment [Esposti Ongaro et al. 2007]. A parallel communications layer based on the Message Passing Interface (MPI) protocol and a friendly input/output interface make the new PDAC code portable on most parallel (shared- and distributed-memory) architectures and transparent to the programmers and the users. The new code is thus able to exploit the peak performance of large supercomputers and workstation clusters. In detail the code was run on a Linux cluster with 66 AMD Opteron CPUs at 1 GHz and 52 GB RAM, interconnected with a low-latency Myrinet network. On this machine, 3D runs took about 2500 total CPU hours.

Acknowledgements: This research was made possible by grants from the National Science Foundation (EAR-03-10329 to AC, EAR-04-08709 to BV) and the European Commission (Project EXPLORIS n. EVR1-CT-2002-40026 to AN) and the Dipartimento della Protezione Civile, Italy (to TEO and AN). Computer time was provided by INGV Pisa. We thank Greg Valentine and Ken Wohletz for very useful comments on an earlier draft as well as Gert Lube and anonymous reviewer for their contributions. We acknowledge insights gained from previous work by colleagues at the Montserrat Volcano Observatory, and those involved in the preparation of Geological Society Memoir 21.

References Cited

Barclay, J., M. R. Carroll, M. J. Rutherford, M. D. Murphy, J. D. Devine, J. Gardner J, and R. S. J. Sparks (1998) Experimental phase equilibria constraints on pre-eruptive storage conditions of the Soufrière Hills magma. *Geophys. Res. Lett., 25*: 3437-3440

Barsotti, S. (2002) Modelli di turbolenza per la simulazione delle eruzioni vulcaniche esplosive. Univ. di Pisa. Master Thesis, 107 pp (in Italian).

Baxter, P. J., R. Boyle, P. Cole, A. Neri, R. Spence, and G. Zuccaro (2005), The impacts of pyroclastic surges on buildings at the eruption of the Soufrière Hills volcano, Montserrat, *Bull. Volcanol., 67*, 292-313.

Belousov, A. (1996), Pyroclastic deposits of March 30, 1956 directed blast at Bezymianny volcano, *Bull. Volcanol.*, *57*, 649-662.

Belousov, A.B., B. Voight, and M. Belousova (2007), Directed blasts and blast-generated pyroclastic currents: a comparison of the Bezymianny 1956, Mount St. Helens 1980, and Soufrière Hills, Montserrat 1997 eruptions and deposits, *Bull. Volcanol.,* 69: 701-740.

Brantley, S. R., and R. B. Waitt (1988) Interrelations among pyroclastic surge, pyroclastic flow, and lahars in the Smith Creek valley during the first minutes of 18 May 1980 eruption of Mount St. Helens, USA. *Bull. Volcanol., 50*: 304-326

Bursik, M. I., A. Kurbatov, M. Sheridan, and A. W. Woods (1998) Transport and deposition in the May 18 1980 Mount St Helens blast, *Geology 26 (2)*: 155-158

Chojnicki, K., A. B. Clarke, and J. C. Phillips (2006), A shock-tube investigation of the dynamics of gas-particle mixtures: Implications for explosive volcanic eruptions, *Geophysical Research Letters*, *33*(15): L15309-

Clarke, A.B., B. Voight, A. Neri, and G. Macedonio, (2002a) Transient dynamics of vulcanian explosions and column collapse, *Nature*, *415*, 897-901.

Clarke, A.B., A. Neri, G. Macedonio, B. Voight, and T. H. Druitt (2002b), Computational modelling of the transient dynamics of the August 1997 Vulcanian explosions at Soufrière Hills volcano, Montserrat, in *The Eruption of Soufrière Hills Volcano, Montserrat, From 1995 to 1999*, edited by T. H. Druitt and B. P. Kokelaar, *Geol. Soc. Mem.*, *21*, 319-348.

Crandell D. R., and R. Hoblitt (1986), Lateral blasts at Mount St. Helens and hazard zonation, *Bull. Volcanol.*, *48*, 27-37.

Dartevelle, S. (2004), Numerical modeling of geophysical granular flows: 1. A comprehensive approach to granular rheologies and geophysical multiphase flows, *Geochem. Geophys. Geosyst.*, *5*, Q08003, doi:10.1029/2003GC000636.

Dartevelle, S., W. I. Rose, J. Stix, K. Kelfoun, and J. W. Vallace (2004), Numerical modeling of geophysical granular flows: 2. Computer simulations of plinian clouds and pyroclastic flows and surges, *Geochem. Geophys. Geosyst. 5*, doi:10.1029/3003GC000637.

De' Michieli Vitturi M., T. Esposti Ongaro, A. Neri, M.V. Salvetti, and F. Beux, (2007) An immersed boundary method for compressible multiphase flow: application to the dynamics of pyroclastic density currents, *Comput. Geosci.,11*:183-198, doi:10.1007/s10596-007-9047-9.

Dobran, F., A. Neri, and G. Macedonio (1993), Numerical simulation of collapsing volcanic columns, *J. Geophys. Res.*, *98*, 4231-4259.

Druitt, T. H. (1992) Emplacement of the 18 May 1980 lateral blast deposit ENE of Mount St. Helens, Washington. *Bull. Volcanol., 54*: 554573

Druitt, T. H., et al. (2002), Episodes of cyclic Vulcanian explosive activity with fountain collapse at Soufrière Hills volcano, Montserrat, in *The Eruption of Soufrière Hills Volcano, Montserrat, From 1995 to 1999*, edited by T. H. Druitt and B. P. Kokelaar, *Geol. Soc. Mem.*, *21*, 281-306.

Dufek, J., and G. W. Bergantz (2007), Suspended load and bed-load transport of particle-laden gravity currents: the role of particle bed interaction, *Theoretical and Computational Fluid Dynamics*, 21(2):119-145, doi:10.1007/s00162-007-0041-6

Esposti Ongaro, T., A. Neri, M. Todesco, and G. Macedonio (2002), Pyroclastic flow hazard assessment at Vesuvius (Italy) by using numerical modeling. II. Analysis of flow variables. *Bull. Volcanology 64*:178-191.

Esposti Ongaro, T., A. Clarke, A. Neri, and B. Voight (2005), Multiphase numerical simulations of directed blasts and their pyroclastic density currents: pressurization and topographic controls for the December 1997 Boxing Day event, Montserrat, and the 1902 events at Montagne Pelee, Martinique, paper presented at Soufrière Hills Volcano - Ten Years On…Scientific Conference, Montserrat, B.W.I.

Esposti Ongaro, T., M. Pelanti, A. Neri, and R. LeVeque, (2006b) Shock-wave pattern and atmospheric signature of underexpanded volcanic jets: a comparative study using two numerical multiphase flow models, Workshop on The physics of fluid oscillation in volcanic systems, Lancaster (UK), September 2006.

Esposti Ongaro, T., A. Neri, C. Cavazzoni, G. Erbacci, and M.V. Salvetti, (2007) A parallel multiphase flow code for the 3D simulation of explosive volcanic eruptions. *Parallel Computing,* doi:10.1016/j.parco.2007.04.003.

Fisher, R. V., H. Glicken, and R. P. Hoblitt (1987) May 18, 1980, Mount St. Helens deposits in South Coldwater Creek, Washington. *J. Geophys. Res., 92*: 10267-10283

Fisher, R. V. (1990), Transport and deposition of a pyroclastic surge across an area of high relief: the 18 May 1980 eruption of Mount St. Helens, Washington, *Geol. Soc. Am. Bull.*, *102*, 1038-1054.

Gidaspow, D. (1994), *Multiphase Flow and Fluidization: Continuum and Kinetic Theory Descriptions*, Academic Press, San Diego, Calif.

Gidaspow, D., and M. Driscoll (2007) Porosity and pressure waves in a fluidized bed of FCC particles, *Powder Technology*, in press.

Glasstone S., and P. J. Dolan (1977) The effects of nuclear weapons. US Dept Defense and US Energy Res Develop Admin, US Gov Printing Office, Washington DC, third ed, pp 1-653

Glicken, H. (1998) Rockslide-debris avalanche of May 18, 1980, Mount St. Helens volcano, Washington. *Bull. Geol. Soc. Japan, 49*: 55-106

Gorshkov, G. S. (1959) Gigantic eruption of the Bezymianny volcano. *Bull. Volcanol., 20*: 77-109

Harlow, F. H., and A. A. Amsden (1975), Numerical calculation of multiphase fluid flow, *J. Comput. Phys.*, *17*, 19-52.

Hart, K., S. Carey, and H. Sigurdsson (2004), Discharge of pyroclastic flows into the sea during the1996-1998 eruptions of the Soufriere Hills volcano, Montserrat, *Bull. Volcanol.*, *66*, 599-614.

Hickson, C. (1990), The May 18, 1980 Eruption of Mount St Helens, Washington State: A synopsis of events and review of Phase I from an eyewitness perspective, *Geoscience Canada*, *17*, No. 3,127-130.

Hoblitt, R.V. (2000), Was the 18 May 1980 lateral blast at Mt. St. Helens the product of two explosions, *Phil. Trans. Royal Soc. London*, *358*, 1639-1661.

Hoblitt, R.V., C. D. Miller, and J. W. Vallance (1981), Origin and stratigraphy of the deposit produced by the May 18 directed blast, in *The 1980 Eruptions of Mount St. Helens, Washington*, edited by P. W. Lipman and D. R. Mullineaux, *U.S. Geol. Surv. Prof. Pap.*, *1250*, 401-419.

Kieffer, S. W. (1981), Fluid dynamics of the May 18 blast at Mount St. Helens, in *The 1980 Eruptions of Mount St. Helens, Washington*, edited by P. W. Lipman and D. R. Mullineaux, *U.S. Geol. Surv. Prof. Pap.*, *1250*, 379-401.

Kieffer, S. W. (1984) Factors governing the structure of volcanic jets. In: Explosive volcanism: inception, evolution, and hazards. National Academy Press, Washington, pp 143-157

Kieffer, S. W., and B. Sturtevant (1984) Laboratory studies of volcanic jets. *J. Geophys. Res.*, *89*: 8253-8268

Kieffer, S. W., and B. Sturtevant (1988) Erosional furrows formed during the lateral blast at Mount St Helens, May 18 1980. *J. Geophys. Res.*, *93*: 14793-14816

Lipman, P. W., and D. R. Mullineaux (eds) (1981) The 1980 eruptions of Mount St. Helens, Washington. *US Geol. Surv. Prof. Pap. 1250*: 69-86

Mayberry, G. C., W. I. Rose, and G. J. S. Bluth (2002) Dynamics of volcanic and meteorological clouds produced on 26 December (Boxing Day) 1997 at Soufriere Hills Volcano, Montserrat. In: Druitt TH, Kokelaar BP (eds) The eruption of Soufrière Hills volcano, Montserrat, from 1995 to 1999. *Mem. Geol. Soc. London 21*: 539-556

Melnik, O., and R. S. J. Sparks RSJ (1999) Non-linear dynamics of lava dome extrusion. *Nature, 402*: 37-41

Melnik, O., and R. S. J. Sparks (2002) Dynamics of magma ascent and lava extrusion at the Soufrière Hills volcano, Montserrat. In: Druitt TH, Kokelaar BP (eds) The eruption of Soufrière Hills volcano, Montserrat, from 1995 to 1999. *Mem. Geol. Soc. London, 21*: 153 - 171

Minor, J. (1994) Windborne debris and the building envelope. *J. Wind Engineering and Industrial Aerodynamics* 53:207-227.

Moore, J. G., and C. J. Rice (1984), Chronology and character of the May 18, 1980, explosive eruptions of Mount St. Helens, in *Explosive Volcanism: Inception, Evolution and Hazards*, pp. 133-142, National Academy Press, Washington, D.C.

Moore J. G., and T. W. Sisson (1981) Deposits and effects of the May 18 pyroclastic surge. In: Lipman PW, Mullineaux DR (eds) The 1980 eruptions of Mount St. Helens, Washington. *US Geol. Surv. Prof. Pap. 1250*: 421- 438.

Nairn, I. A. (1976) Atmospheric shock waves and condensation clouds from Ngauruhoe explosive eruptions, *Nature*, *259*, 190-192.

Nairn, I. A., and S. Self (1978) Explosive avalanches and pyroclastic flows from Ngauruhoe, 1975, *J. Volcanol. Geotherm. Res.*, *3*, 39-60.

Neri, A., and D. Gidaspow (2000), Riser hydrodynamics: Simulation using kinetic theory. *AIChE J.*, 42, 52-67.

Neri, A., and G. Macedonio (1996), Numerical simulation of collapsing volcanic columns with particles of two sizes, *J. Geophys. Res.*, *101*, 8153-8174.

Neri A., T. Esposti Ongaro, G. Macedonio, and D. Gidaspow (2003), Multiparticle simulation of collapsing volcanic columns and pyroclastic flows, *J. Geophys. Res.*, 108 (B4), 2202, doi :10.1029/2001JB000508.

Neri, A., T. Esposti Ongaro, G. Menconi, M. De'Michieli Vitturi, C. Cavazzoni, G. Erbacci, and P. J. Baxter (2007). 4D simulation of explosive eruption dynamics at Vesuvius, *Geophys. Res. Lett.*, Vol. 34, L04309, doi:10.1029/2006GL028597.

Pace, J.C., P. Vogt, J. S. Ellis, B. Voight, and R. Lefevre, 1998. ARAC simulations of the ash plume from the December 1997 eruption of the Soufriere Hills Volcano, Montserrat. International Meteorological Conference, Houston. 6 pp.

Ritchie, L., P. Cole, and R. S. J. Sparks (2002), Sedimentology of pyroclstic density current deposits generated by the December 26, 1997 eruption at the Soufrière Hills volcano, Montserrat, in *The Eruption of Soufrière Hills Volcano, Montserrat, From 1995 to 1999*, edited by T. H. Druitt and B. P. Kokelaar, *Geol. Soc. Mem.*, *21*, 435-456.

Rivard, W. C., and M. D. Torrey (1977), K-FIX: A computer program for transient, two-dimensional, two-fluid flow, *LA-NUREG* 6623, Los Alamos Natl. Lab., Los Alamos, N.M.

Robertson, R., P. Cole, R. S. J. Sparks, C. Harford, A. M. Lejeune, W. J. McGuire, A. D. Miller, M. D. Murphy, G. Norton, N. F. Stevens, and S. R. Young (1998) The explosive eruption of Soufrière Hills volcano, Montserrat, West Indies, September 17, 1996. *Geophys. Res. Lett., 25*: 3429-3433

Sisson, T. W. (1995) Blast ashfall deposit of May 18, 1980 Mount St Helens, Washington. *J. Volcanol. Geotherm. Res., 66*: 203-216

Sparks, R. S. J. (1997) Causes and consequences of pressurization in lava dome eruptions. *Earth Planet. Sci. Lett., 150*: 177-189

Sparks, R. S. J., M. Bursik, S. N. Carey, J. S. Gilbert, L. S. Glaze, H. Sigurdsson, and A. W. Woods (1998) *Volcanic plumes*. Wiley, New York

Sparks, R. S. J., et al. (2002), Generation of a debris avalanche and violent pyroclastic density current: the Boxing Day eruption of 16 December 1997 at the Soufrière Hills volcano, Montserrat, in *The Eruption of Soufrière Hills Volcano, Montserrat, From 1995 to 1999*, edited by T. H. Druitt and B. P. Kokelaar, *Geol. Soc. Mem.*, *21*, 409-434.

Valentine, G. A. (1998a), Damage to structures by pyroclastic flows and surges, inferred from nuclear weapons effects, *J. Volcanol. Geotherm. Res.*, *87*, 117-140.

Valentine, G.A. (1998b), Eruption column physics, in *From magma to tephra. Modelling physical processes of explosive volcanic eruptions*. Eds. A. Freundt and M. Rosi, Elsevier

Valentine, G. A., and K. H. Wohletz (1989), Numerical models of Plinian eruption columns and pyroclastic flows, *J. Geophys. Res.*, *94*, 1867-1887.

Voight, B. (1981), Time scale for the first movements of the May 18 eruption, in *The 1980 Eruptions of Mount St. Helens, Washington*, edited by P. W. Lipman and D. R. Mullineaux, *U.S. Geol. Surv. Prof. Pap.*, *1250*, 69-86.

Voight, B., H. Glicken, R. J. Janda, and P. M. Douglass (1981) Catastrophic rockslide avalanche of May 18. In: Lipman PW, Mullineaux DR (eds) The 1980 eruptions of Mount St. Helens, Washington. *US Geol. Surv. Prof. Pap.*, *1250*: 347-377

Voight, B., H. Glicken, R. J. Janda, P. M. Douglass (1983) Nature and mechanics of the Mount St Helens rockslide-avalanche of 18 May 1980. *Geotechnique, 33*:243-273

Voight, B., R. S. J. Sparks, A. D. Miller, R. C. Stewart, R. P. Hoblitt, A. Clarke, J. Ewart, W. P. Aspinall, B. Baptie, E. S. Calder, P. Cole, T. H. Druitt, C. Hartford, R. A. Herd, P. Jackson, A. M. Lejeune, A. B. Lockhart, S. C. Loughlin, R. Luckett, L. Lynch, G. E. Norton, R. Robertson, I. M. Watson, R. Watts, and S. R. Young (1999), Magma flow instability and cyclic activity at Soufriere Hills volcano, Montserrat, British West Indies, *Science*, *283*(5405):1138 – 1142, doi: 10.1126/science.283.5405.1138

Voight, B., J. C. Komorowski, G. Norton, A. Belousov, M. Belousova, G. Boudon, P. Francis, W. Franz, S. Sparks, and S. Young (2002), The 1997 Boxing Day sector collapse and debris avalanche, Soufrière Hills Volcano, Montserrat, B.W.I., in *The Eruption of Soufrière Hills Volcano, Montserrat, From 1995 to 1999*, edited by T. H. Druitt and B. P. Kokelaar, *Geol. Soc. Mem.*, *21*, 363-407.

Waitt, R. B. J. (1981), Devastating pyroclastic density flow and attendant air fall of May 18 stratigraphy and sedimentology of deposits, in *The 1980 Eruptions of Mount St. Helens, Washington*, edited by P. W. Lipman and D. R. Mullineaux, *U.S. Geol. Surv. Prof. Pap.*, *1250*, 439-458.

Walker, G. P. L., and L. A. McBroome (1983) Mount St. Helens 1980 and Mount Pelée 1902 – flow or surge? *Geology, 11*: 571-574

Wallis, G. B., (1969). *One-Dimensional Two-Phase Flow*. McGraw-Hill

Wills, J. A. B., B. E. Lee, and T. A. Wyatt (2002). A model of wind-borne debris damage. *J. Wind Engineering and Industrial Aerodynamics* 90:555-565.

Wohletz, K. H. (1998), Pyroclastic surges and compressible two-phase flow, in *From Magma to Tephra*, edited by A. Freundt and M. Rosi, pp. 247-312, Elsevier, Amsterdam.

Wohletz, K. H., T. R. McGetchin, M. T. Sandford II, and E. M. Jones (1984), Hydrodynamic aspects of caldera-forming eruptions: Numerical model, *J. Geophys. Res.*, *89*, 8269-8285.

Wohletz, K. H., G. A. Valentine (1990) Computer simulations of explosive volcanic eruptions. In: Ryan, MP (ed) *Magma Transport and Storage*. Wiley, New York, pp 113-135

Woods, A. W. (1995), A model of vulcanian explosions, *Nuc. Eng. And Des., 155*, 345-357. (1995).

Woods, A. W., R. S. J. Sparks, J. Batey, C. Gladstone, L. J. Ritchie, and M. Bursik (2002), The generation of vertically stratified pyroclastic density currents by rapid decompression of a pressurised volcanic dome on 26 December (Boxing Day) 1997 at Soufrière Hills volcano, Montserrat, in *The Eruption of Soufrière Hills Volcano, Montserrat, From 1995 to 1999*, edited by T. H. Druitt and B. P. Kokelaar, *Geol. Soc. Mem.*, *21*, 457-465.

Young , S.R., P. Francis, J. Barclay et al., (1998) Monitoring SO_2 emission at the Soufrière Hills Volcano: implications for changes in eruptive conditions. *Geophys. Res. Lett., 25,* 3681-3684

Young, S. R., B. Voight, J. Barclay, R. A. Herd, J. C. Komorowski, A. D. Miller, R. S. J. Sparks, and R. C. Stewart (2002), Hazard implications of small-scale edifice instability and sector collapse; a case history from Soufriere Hills Volcano, Montserrat, in *The Eruption of Soufrière Hills Volcano, Montserrat, From 1995 to 1999*, edited by T. H. Druitt and B. P. Kokelaar, *Geol. Soc. Mem.*, *21*, 349-461.

Table captions

Table 1. List of the main parameters used in 2D and 3D simulations. κ is the porous dome permeability, V_{DRE} is the Dense Rock Equivalent volume of the dome, R_d is the resulting dome radius, M is the solid mass in the dome, α the porosity (void fraction) and E is the expansion energy per unit mass assuming an adiabatic or isothermal expansion (see text). The total mass in the 2D runs is multiplied by a factor accounting for the asymmetric distribution of the deposit over a sector of 70°.

Table 2. List of the main simulation outputs from 2D simulations. H_b is the maximum burst height above the dome (see Figs. 3, 5, 7), $U_{b,g}$ is the gas *burst* velocity, $U_{b,p}$ is the three particles *burst* velocity, U_f is the average velocity of the PDC after collapse, T_p is the time at which the phoenix cloud form from the PDC front, E is the percentage of pyroclasts elutriated at the final simulation time, Rm_{max}, Um_{max}, Pd_{max} are the maximum mixture density, velocity and dynamic pressure at 10m and 2, 3 and 4 km from the vent (see Fig. 11), Pd_{SP} is the maximum dynamic pressure at St. Patrick village (R=3.4 km, see Fig. 12).

Figure captions

Figure 1. The area affected by the 1997 Boxing Day lateral blast on Montserrat, view from south. a) before: foreground, St. Patricks village (left) and White River valley; background, SHV. b) after, showing debris avalanche deposit in and near the valley, and widespread blanket of PDC deposits over 70^o sector. St. Patricks at lower left is completely destroyed.

Figure 2. Distribution of 1997 Boxing Day deposits (from Sparks et al., 2002). A-A' marks the profile used in 2D runs A, B & C.

Figure 3. a) Initial expansion of 2D simulation A-2D ($V_{DRE} = 5 \times 10^6$ m^3, K = 10^{-12} m^2). Contours are $\log_{10}$ of particle volume fraction. Initial condition, 2 s, 5 s and 12 s into simulation. By 12s the plume exhibits the collapse phase. b) Trajectories of fluid particles from 0 to 15s defining the burst phase and collapse phase of eruption.

Figure 4. Simulation A-2D ($V_{DRE} = 5 \times 10^6$ m^3, K = 10^{-12} m^2). Contours are $\log_{10}$ of particle volume fraction (color map as in Fig. 3a). At 10s the burst phase has ceased and the PDC moves along the volcanic slope. At 20s the PDC head forms by the effect of the air entrainment at 1.5 km. At 40s in the PDC phase, the leading edge has thickened and most of the solid mass has entered the PDC. By 90s the PDC has progressed beyond the shoreline and further thickening of the leading edge is evident. By 180 s the PDC has reached 8 km and segregated fines are forming a co-PDC plume, with minor plumes at the trailing edge. At 240s, co-PDC plumes are well-developed and vertical motion dominates. Animated contours can be viewed on Movie S1 in the on-line auxiliary material.

Fig 5. a) Initial expansion of simulation B-2D ($V_{DRE} = 10 \times 10^6$ m^3 , K = 10^{-12} m^2). Contours are $\log_{10}$ of particle volume fraction. Initial condition, 2 s, 5 s and 12 s into simulation. By 12s the plume exhibits the collapse phase. b) Trajectories of the fluid particles from 0 to 15s, defining the burst phase and collapse phase of eruption. The initial phase is not greatly affected by total mass (compare to Fig. 3a and 3b).

Figure 6. Results of B-2D ($V_{DRE} = 10 \times 10^6$ m^3 , K = 10^{-12} m^2). Contours are $\log_{10}$ of particle volume fraction (color map as in Fig. 5a). From 0 to 40s the dynamics is similar to A-2D, but the PDC front is more advanced. At 40s in the PDC phase, the leading edge has thickened. By 90 s the

PDC has progressed well beyond the shoreline with further thickening and broadening of the leading front. At 180s the increased dome mass and inertia results in high-speed runout beyond the computational limit of 8 km (PDC motion continues). Deposition is offshore. Buoyant co-PDC plumes are in the early stages of development. Animated contours can be viewed on Movie S2 in the on-line auxiliary material.

Figure7. a) Initial expansion of 2D simulation C-2D ($V_{DRE} = 5 \times 10^6$ m^3 **,** K = 10^{-14} m^2). Contours are $\log_{10}$ of particle volume fraction . Initial condition, 2 s, 5 s and 12 s into simulation. The initial phase is strongly affected by initial total specific gas energy (compare Fig. 3). b) Trajectories of fluid particles from 0 to 10s, defining the burst phase and collapse phase of eruption (please notice the change in the axis scale with respect to Figs. 3b) and 5b).

Figure 8. Pressure perturbation at ground level and different radial distances (from 1 to 3.5 km) produced by the exploding dome in simulation C-2D.

Figure 9. Results of C-2D ($V_{DRE} = 5 \times 10^6$ m^3 **,** K = 10^{-14} m^2). Contours are $\log_{10}$ of particle volume fraction (color map as in Fig. 5a). At 10s the pyroclastic material is expanding in the atmosphere (burst phase) by the effect of the high initial gas overpressure. At 20s the erupting material is collapsing to the ground forming a PDC. At 40s in the PDC phase, the leading edge has thickened. By 90 s the PDC has progressed past the shoreline with further thickening and broadening of the leading front. By 180 s the PDC has passed 6 km but has stalled and segregated fines are forming a co-PDC plume, with minor plumes at the trailing edge. At 240s, co-PDC plumes are well-developed onshore and vertical motion dominates. Animated contours can be viewed on Movie S3 in the on-line auxiliary material.

Figure 10. a) Front position versus time, and b) Front velocity versus position of simulations A-2D (solid line), B-2D (dashed) and C-2D (dotted). The front is tracked by following the most advanced part of the flow, irrespective of its shape (expanded flow head or thin basal flow).

Figure 11. Time-wise variation of the mixture density (top), mixture velocity (middle) and flow dynamic pressure (bottom) at 2 km (red), 3 km (green) and 4 km (blue) from the source. Values are sampled 10m above the ground level. Plots on the left are results from an erupted mass of $V_{DRE} = 5$

x 10^6 m^3 and different dome permeabilities (A-2D:10^{-12} m^2 - solid line; C-2D: 10^{-14} m^2 - dashed line). Plots on right are results from a higher erupted mass: B-2D (V_{DRE} = 10 x 10^6 m^3) and high dome permeability (10^{-12} m^2).

Figure 12. Flow dynamic properties at St Patricks, 3.4 km from source, resulting from simulations A-2D (solid line), B-2D (dashed) and C-2D (dotted). a) Time-wise variation of the flow dynamic pressure. Values are sampled 10m above the ground level. b) Vertical flow profile at the time of maximum dynamic pressure reported in the legend.

Figure 13. Isocontours [-8:0:-1] of the Log_{10} of the total particle fraction at t=0s, t=5s and t=10s across a vertical section parallel to the Y axis in 3D simulations [X=80700]. The dark solid contour indicates the initial volume of the exploding dome at [X=80690m; Y=46550m; Z=710m]. A) Simulation A-3D (V_{DRE} = 5 x 10^6 m^3**,** K = 10^{-12} m^2); B) B-3D (V_{DRE} = 11 x 10^6 m^3**,** K = 10^{-12} m^2). The sequences can be compared with those in 2D in Fig. 3 and 5 (but the initial position of the dome is somewhat different; see text).

Figure 14. Temporal evolution of 3D pyroclastic dispersal process at 30, 60 and 90s. View from South on 20-m grid DEM. The isosurfaces correspond to the total particle concentrations of 10^{-6} (outer, light brown) and 10^{-2} (inner dark) a) Simulation A-3D (V_{DRE} = 5 x 10^6 m^3**,** K = 10^{-12} m^2); b) Simulation B-3D (V_{DRE} = 11 x 10^6 m^3**,** K = 10^{-12} m^2). Animated contours can be viewed on Movie S4 to S6 in the on-line auxiliary material.

Figure 15. Left panels: Simulation A-3D (V_{DRE} = 5 x 10^6 m^3**,** K = 10^{-12} m^2); Right panels: Simulation B-3D (V_{DRE} = 11 x 10^6 m^3**,** K = 10^{-12} m^2). a,d) Map of the log_{10} of total particle concentration at 10m above ground (the basal cell) at 90 s. Note channelized flow to the east, in Dry Ghaut, which was also recognized in the field. The bold line indicates the boundary of the debris avalanche and blast deposits. b,e) Longitudinal LL' section of the log_{10} of total particle concentration along the flow direction (seen from NW). c-f) Transversal PP' section (seen from NE).

Contours are log_{10} of particle volume fraction. Please note that the color scale is different in the maps from the sections to highlight the weaker variations in the spatial distribution of pyroclasts.

Figure 16 Maps of particle velocity vectors at 90s for simulations A-3D (a) and B-3D (b).

Values are sampled at 10 m above ground level (the basal cell). Points p1-p4 indicates the probe positions for the sampling of Fig. 20 and correspond to central (p1,p3) and peripheral (p2,p4) locations.

Figure 17. Dynamic pressure, mixture density and mixture velocity at 10m above the ground surface at selected locations marked by the dots in Fig. 18. Left) A-3D, Right) B-3D. The value of the maximum dynamic pressure (corresponding to the passage of the PDC head) drastically decreases in moving away from the source, and also from the flow axial region to the flow periphery.

Figure 18. Comparison between the *maximum* dynamic pressure of simulation A-3D (left plots) and B-3D (right plots). a-d) Map view at 10 m above ground surface in the basal cell at 90 s (dome positioned at [X=80690m;Y=46550m;Z=710m]). Solid lines mark longitudinal and transverse sections; b-e) Longitudinal section topography (green) and corresponding simulated maximum dynamic pressure (blue). Please notice that the longitudinal section does NOT correspond to the flow direction or to the steepest slope (see the map). The maximum value of the dynamic pressure drastically decreases with the distance from the source; c-f) Transverse section topography (green) and corresponding simulated maximum dynamic pressure (blue). Peaks in maximum dynamic pressure correspond to deep valleys where particles tend to concentrate, providing evidence that lateral peaks in maximum dynamic pressure are controlled by flow density, rather than flow velocity. The maximum value of the flow dynamic pressure in B-3D is almost double with respect to A-3D due to the increase of the erupting mass.

Figure 19. Mach number distributions for 2D simulations of volcanic blast at Soufrière Hills volcano; Isocontours are traced every 0.2. Maximum values are saturated in red above M=2.0, so that the green color corresponds to M~1 (sonic velocity, white isoline). a-b-c) Simulation B-2D ($V_{DRE} = 10 \times 10^6$ m^3, K=10^{-12}m^2). The collapse phase (t=10s) is characterized by relatively high Mach number (M>2) in a proximal region (R = 500-800 m). High values of the Mach number at 30s correspond to regions at high particle concentration, rather than high velocity. The region affected by locally supersonic flow is limited to R<2.5 km and t = 50s.
d-e-f) Simulation C-2D ($V_{DRE} = 5 \times 10^6$ m^3, K=10^{-14}m^2). Collapse phase shown at 10 s, with transformation to PDC phase nearly complete by 20 s (not shown). Further movement shows thickening and distortion of PDC front edge by air drag. By 30 s, the region for M>1 is limited to a

thin basal patch ~1.5 km from source. By 50 s, with the plume front at the site of destroyed houses (3.4 km), the basal zone of the PDC displays M<0.8, but with high dynamic pressure.

Figure 20. a) Map of the distribution of mixture Mach number at 50s, and at 10m above the ground level, for simulation B-3D ($V_{DRE} = 11 \times 10^6$ m^3**,** $K = 10^{-12}$ m^2). b) Longitudinal section LL' and c) transversal section PP' of the Mach number distribution. Isocontours are shown for every 0.2 change. Maximum value observed is about M~1.0, comparable with that observed in 2D (Fig. 19).

Figure A1. Influence of the mesh size and stretching on the large-scale PDC dynamics at 90s (left plots) and 180s (right plots). Isolines represent the $\log_{10}$ of the total particle volumetric fraction from -8 to -1. a,e) Reference simulation A-2D: *dx* varies from 20 to 100m, vertical minimum size is *dz*=10m (total number of cells $N_t = 8\times10^4$). b,f) Uniform horizontal resolution of 20m, vertical minimum size is *dz*=10m ($N_t = 2\times10^5$). c,g) Uniform horizontal resolution of 20m, vertical minimum size is *dz*=6m ($N_t = 3\times10^5$). d,h) Uniform horizontal resolution of 20m, vertical minimum size is *dz*=20m ($N_t = 1.5\times10^5$).

Figure A2. Influence of the vertical mesh size on the PDC density (a,d), velocity (b,e) and dynamic pressure (c,f) profiles. a, b, and c is at 90 s and 3 km from source; d, e and f is at 90s and 4 km from source. The vertical resolution plotted are 6 m (solid line), 10 m (dashed line), and 20 m (dotted line), with a uniform horizontal resolution of 20 m. The ordinates report the height above the topography in meters (the ground elevation is 161 m at 3 km and 0 m at 4 km).

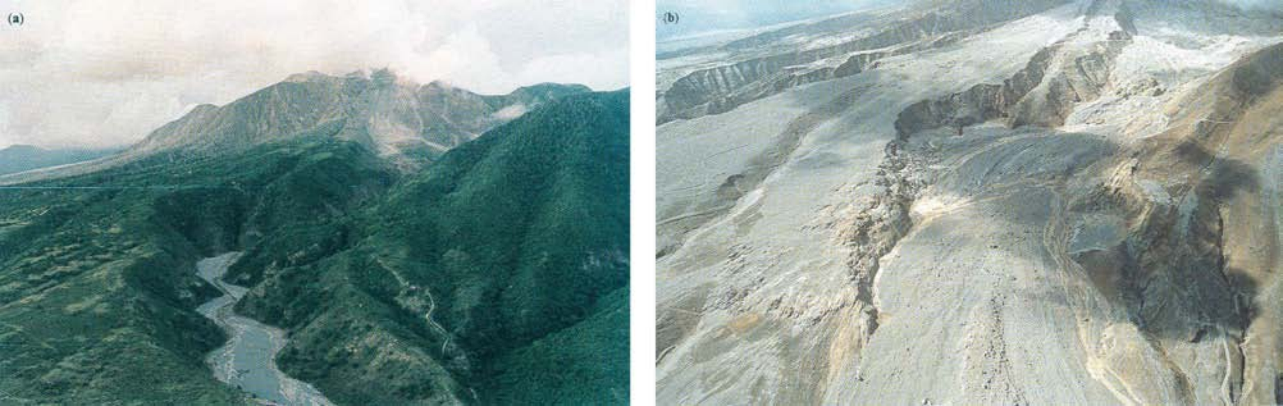
(a)
(b)

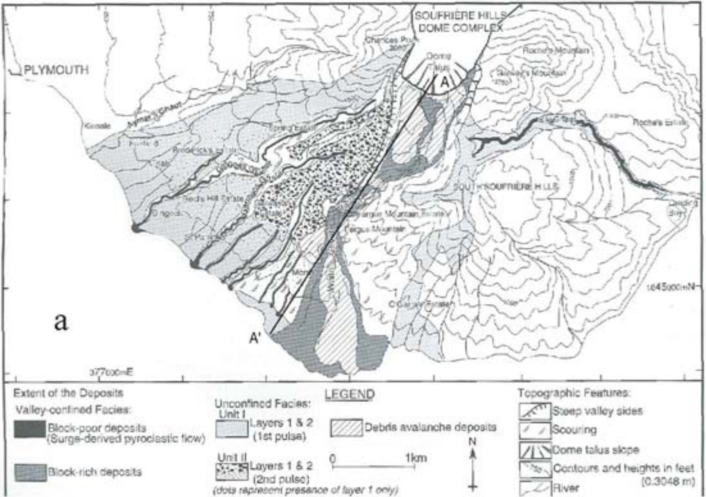
SOUFRIÈRE HILLS
DOME COMPLEX
PLYMOUTH
Dome
Talus
A
Rocho's Mountain
Chances Peak
3000
Kinsale
Spring Estate
Broderick's Estate
Reid's Hill Estate
Roche's Estate
SOUTH SOUFRIÈRE HILLS
Fergus Mountain
O'Garro's Estate
645000mN
a
A'
377000mE
Extent of the Deposits
Valley-confined Facies:
Block-poor deposits
(Surge-derived pyroclastic flow)
Block-rich deposits
Unconfined Facies:
Unit I
Layers 1 & 2
(1st pulse)
Unit II
Layers 1 & 2
(2nd pulse)
(dots represent presence of layer 1 only)
LEGEND
Debris avalanche deposits
0
1km
N
Topographic Features:
Steep valley sides
Scouring
Dome talus slope
Contours and heights in feet
(0.3048 m)
River

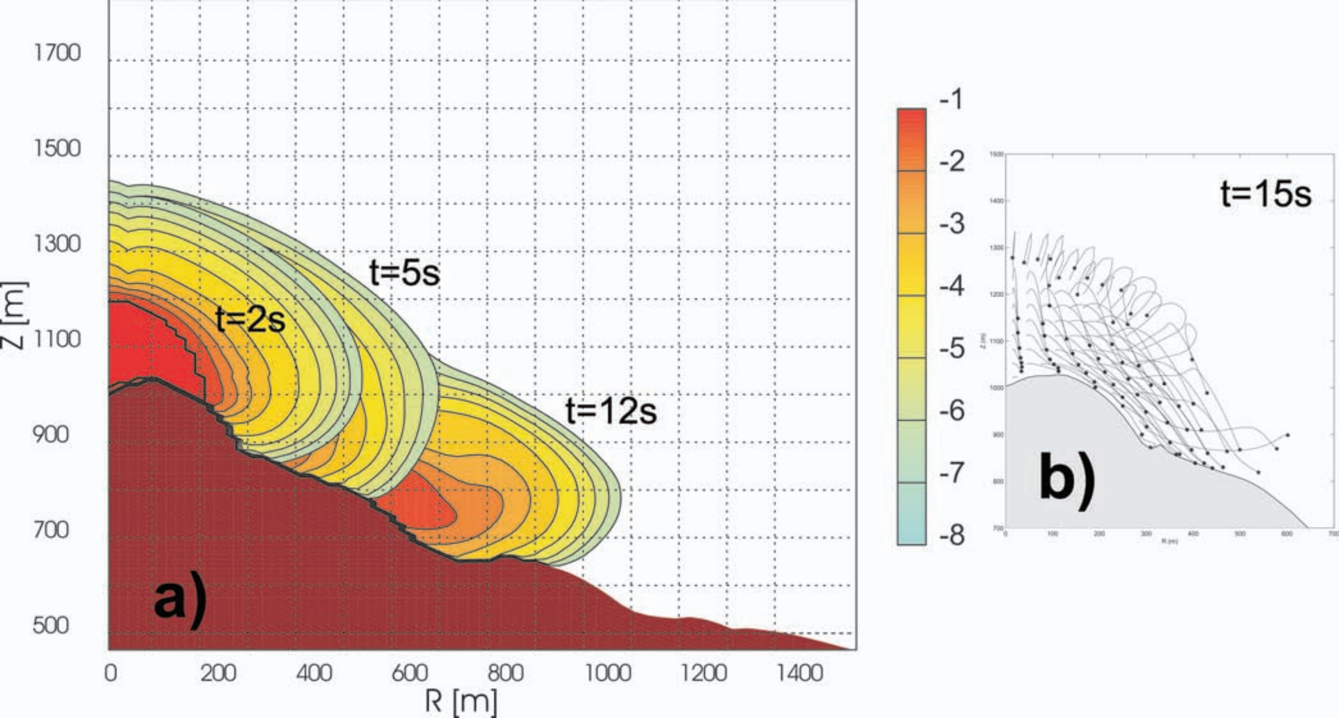
1700
1500
1300
1100
900
700
500
Z [m]
0
200
400
600
800
1000
1200
1400
R [m]
t=2s
t=5s
t=12s
a)
-1
-2
-3
-4
-5
-6
-7
-8
t=15s
b)
1500
1400
1300
1200
1100
1000
900
800
700
Z [m]
0
100
200
300
400
500
600
700
R [m]

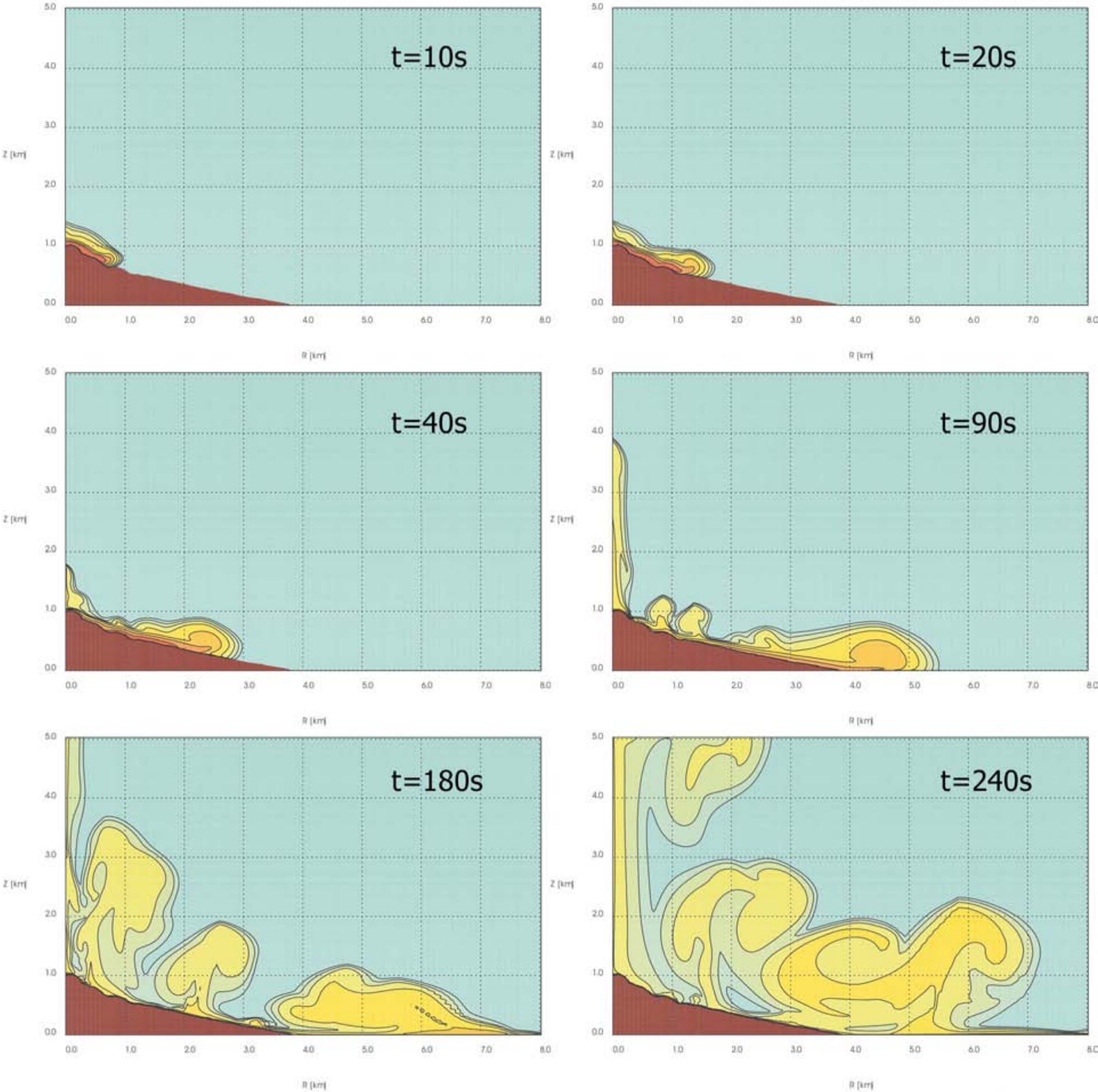
t=10s
t=20s
t=40s
t=90s
t=180s
t=240s
Z [km]
R [km]
0.0
1.0
2.0
3.0
4.0
5.0
6.0
7.0
8.0

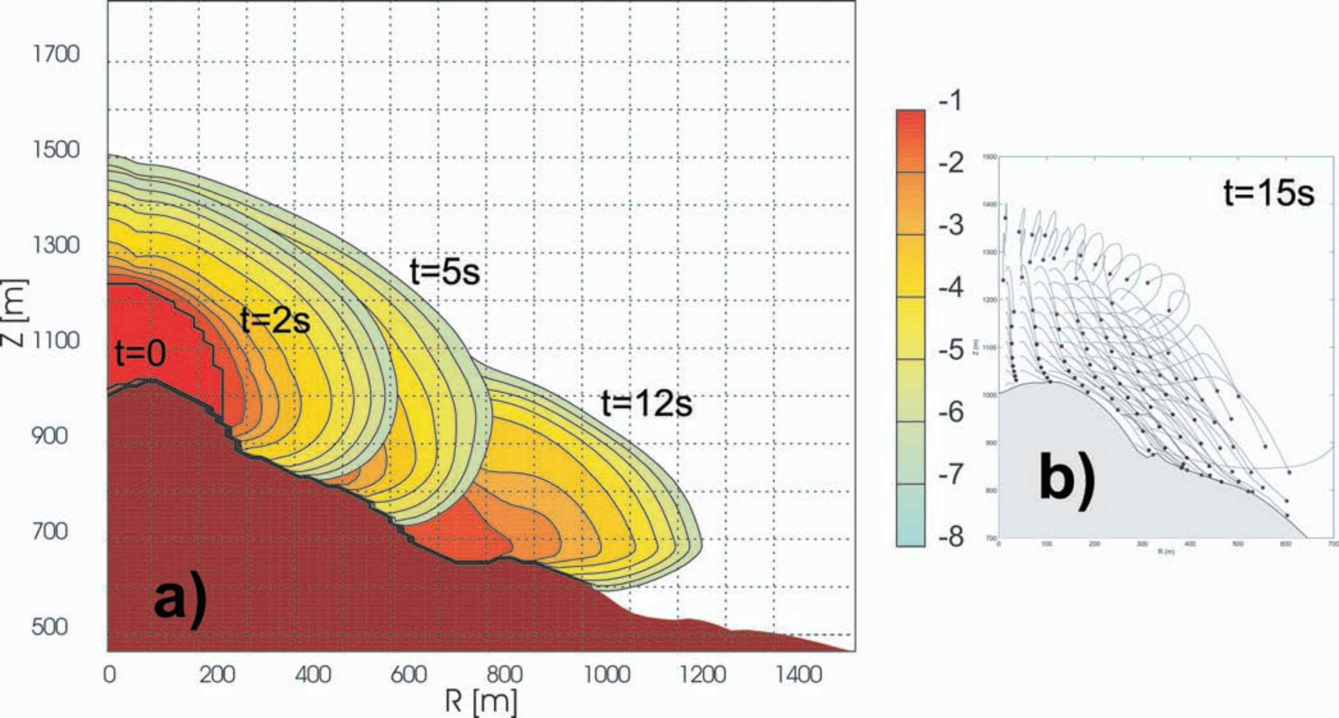
Z [m]
1700
1500
1300
1100
900
700
500
0
200
400
600
800
1000
1200
1400
R [m]
t=0
t=2s
t=5s
t=12s
a)
-1
-2
-3
-4
-5
-6
-7
-8
t=15s
b)
Z (m)
1500
1400
1300
1200
1100
1000
900
800
700
0
100
200
300
400
500
600
700
R (m)

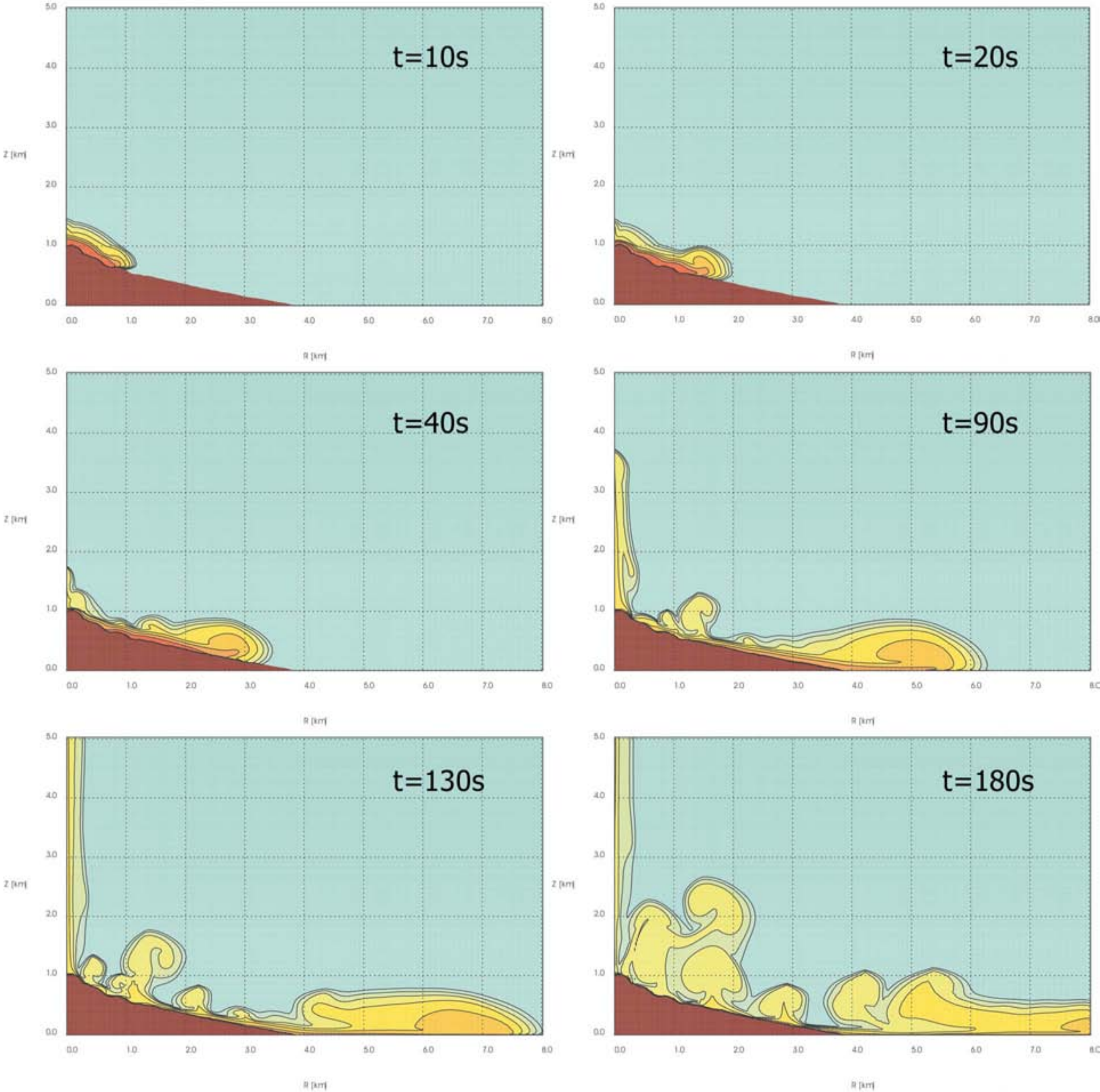
t=10s
t=20s
t=40s
t=90s
t=130s
t=180s
Z [km]
R [km]
0.0
1.0
2.0
3.0
4.0
5.0
6.0
7.0
8.0

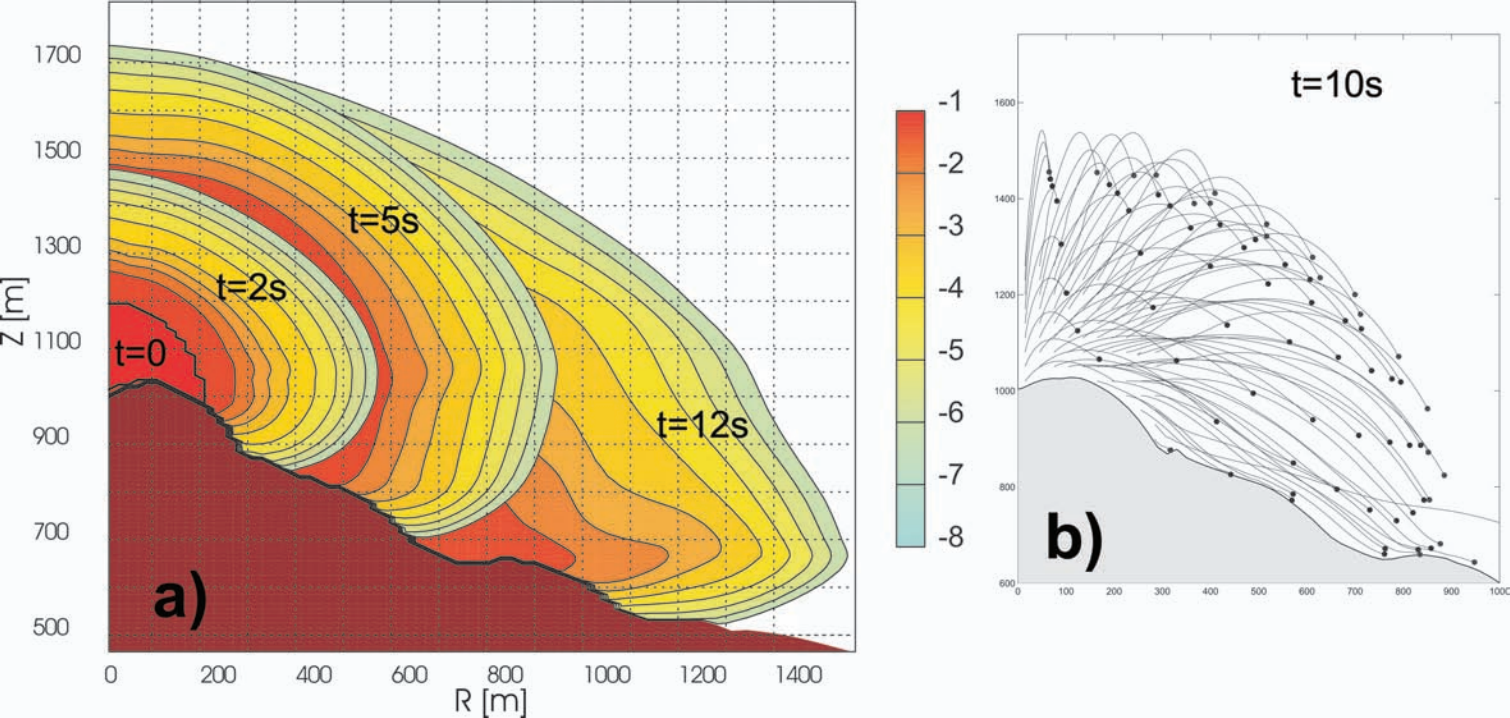
t=0
t=2s
t=5s
t=12s
a)
Z [m]
1700
1500
1300
1100
900
700
500
R [m]
0
200
400
600
800
1000
1200
1400
-1
-2
-3
-4
-5
-6
-7
-8
t=10s
b)
1600
1400
1200
1000
800
600
0
100
200
300
400
500
600
700
800
900
1000

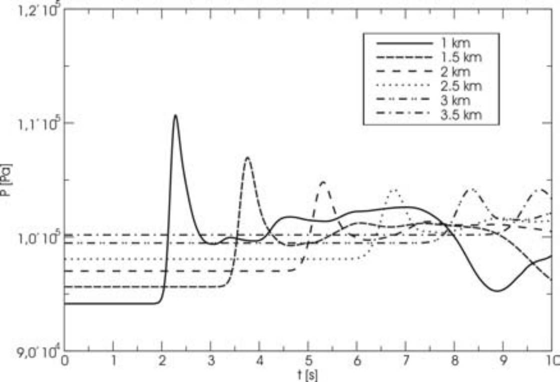
$1,2'10^5$
$1,1'10^5$
$1,0'10^5$
$9,0'10^4$
P [Pa]
0
1
2
3
4
5
6
7
8
9
10
t [s]
1 km
1.5 km
2 km
2.5 km
3 km
3.5 km

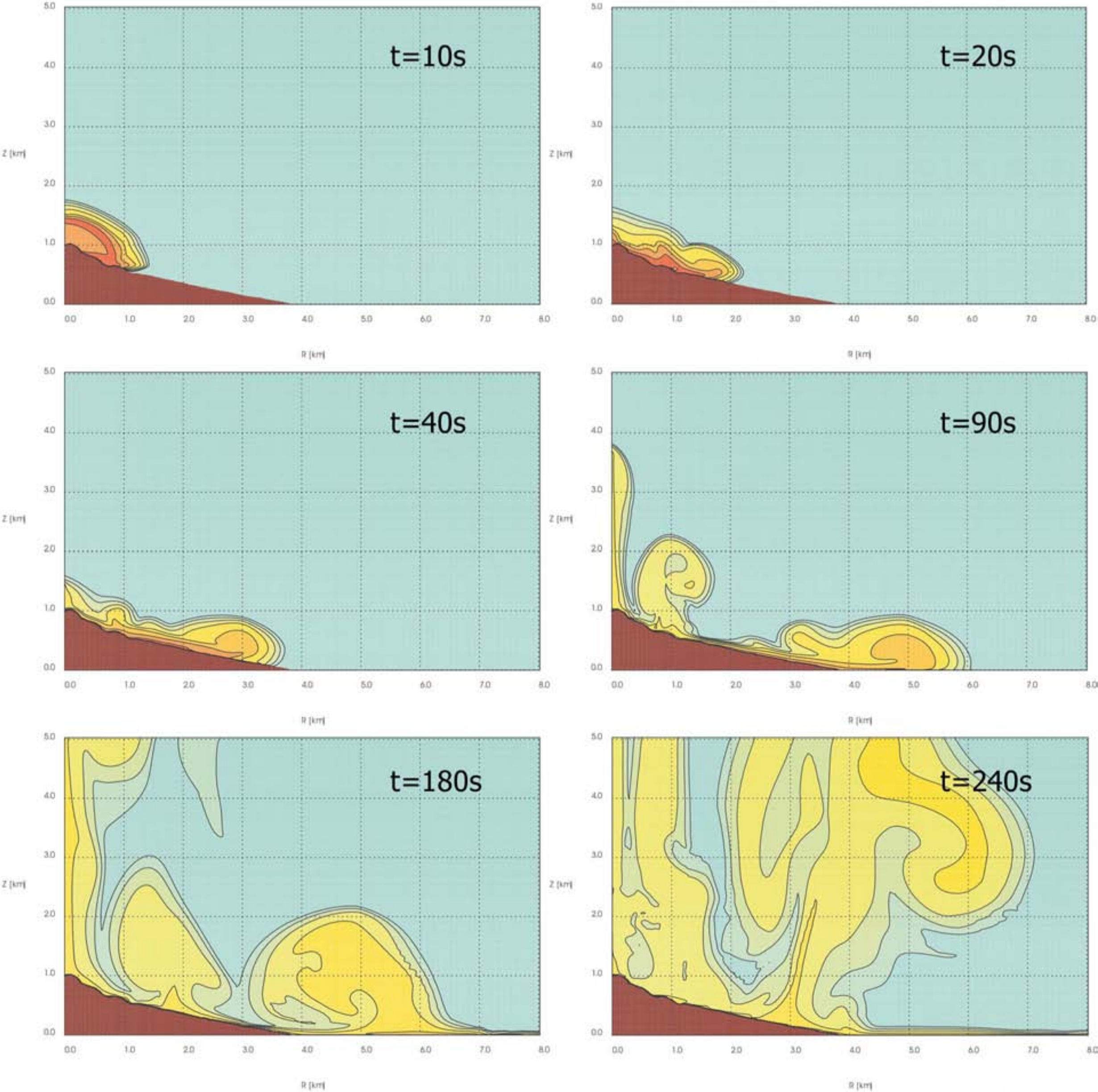
t=10s
t=20s
t=40s
t=90s
t=180s
t=240s
Z [km]
R [km]
0.0
1.0
2.0
3.0
4.0
5.0
6.0
7.0
8.0

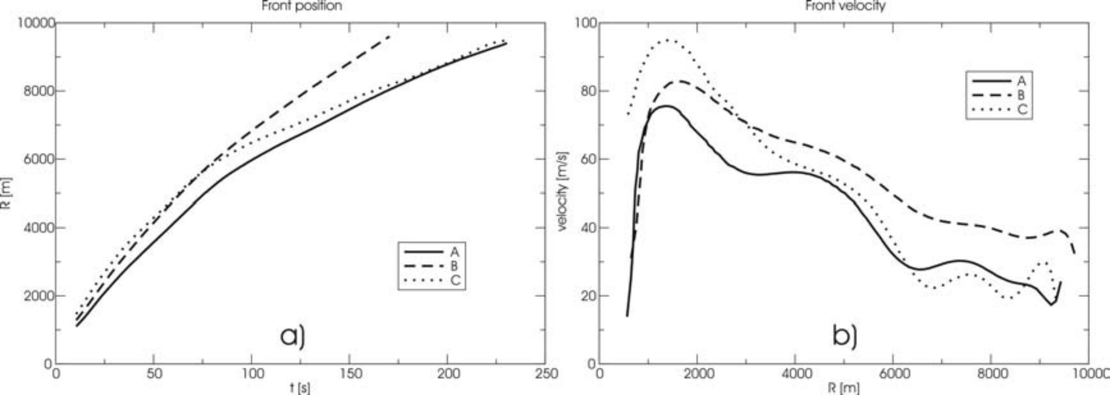
Front position
Front velocity
R [m]
t [s]
velocity [m/s]
R [m]
0
2000
4000
6000
8000
10000
0
50
100
150
200
250
0
20
40
60
80
100
0
2000
4000
6000
8000
10000
A
B
C
A
B
C
a)
b)

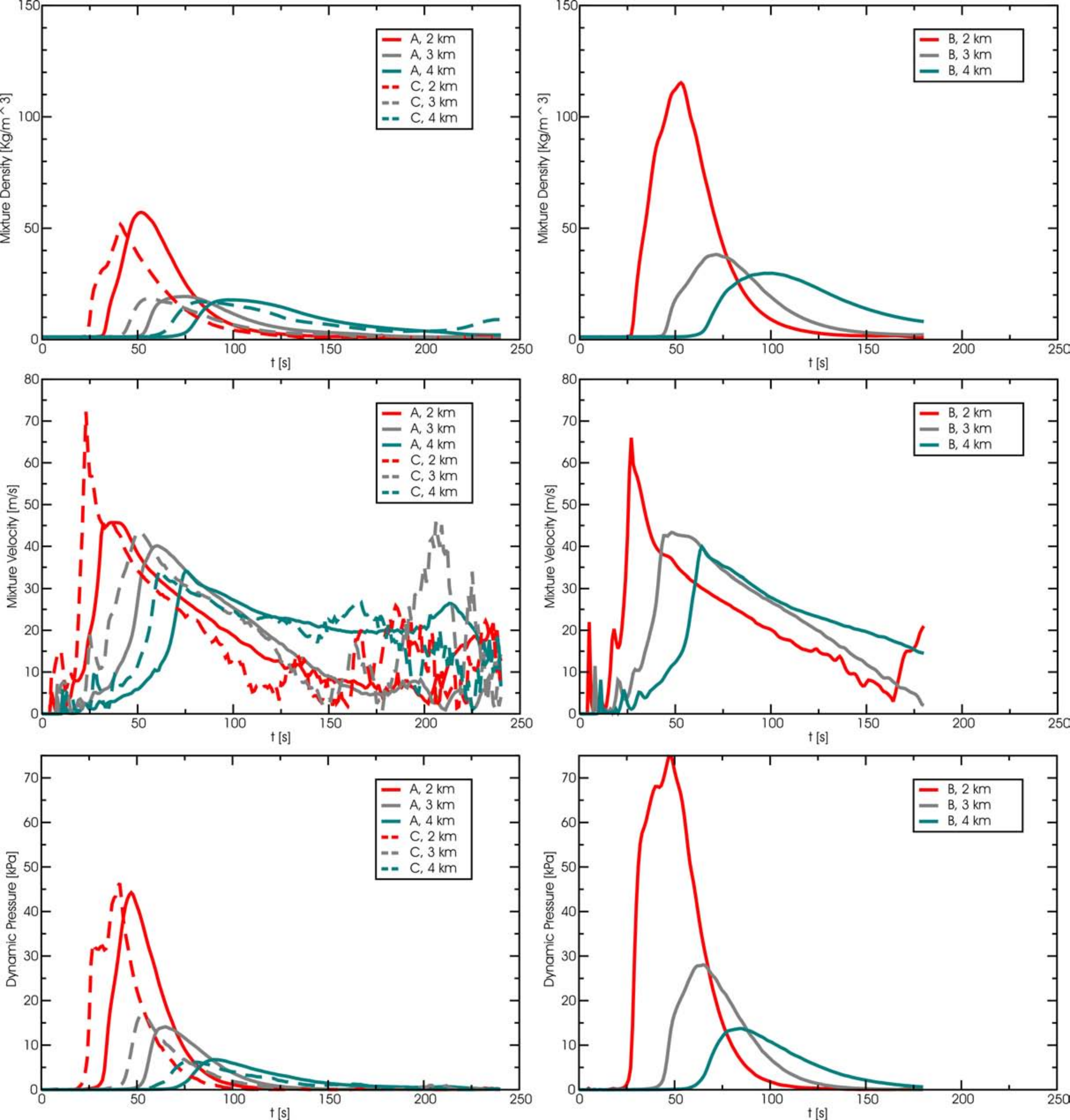
Mixture Density [Kg/m ^ 3]
Mixture Velocity [m/s]
Dynamic Pressure [kPa]
t [s]
A, 2 km
A, 3 km
A, 4 km
C, 2 km
C, 3 km
C, 4 km
B, 2 km
B, 3 km
B, 4 km
0
50
100
150
200
250
10
20
30
40
60
70
80

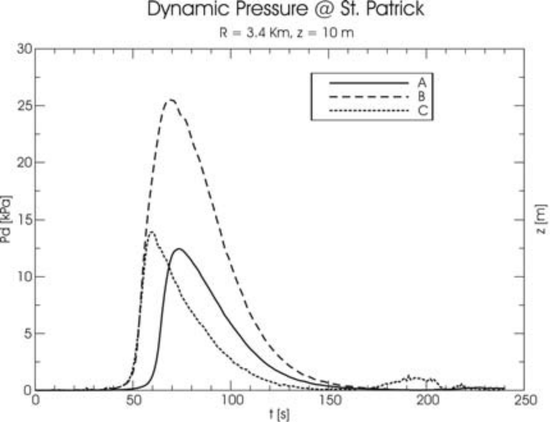
Dynamic Pressure @ St. Patrick

R = 3.4 Km, z = 10 m

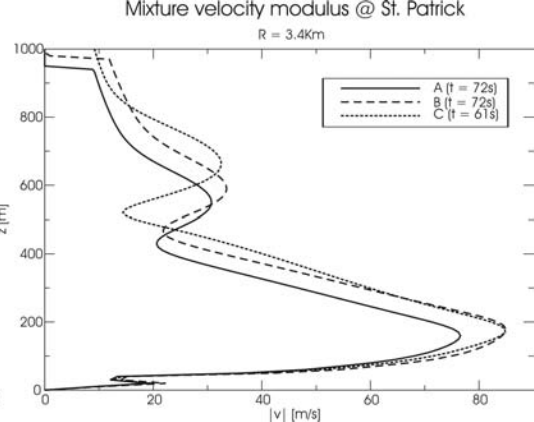
Mixture velocity modulus @ St. Patrick

R = 3.4Km

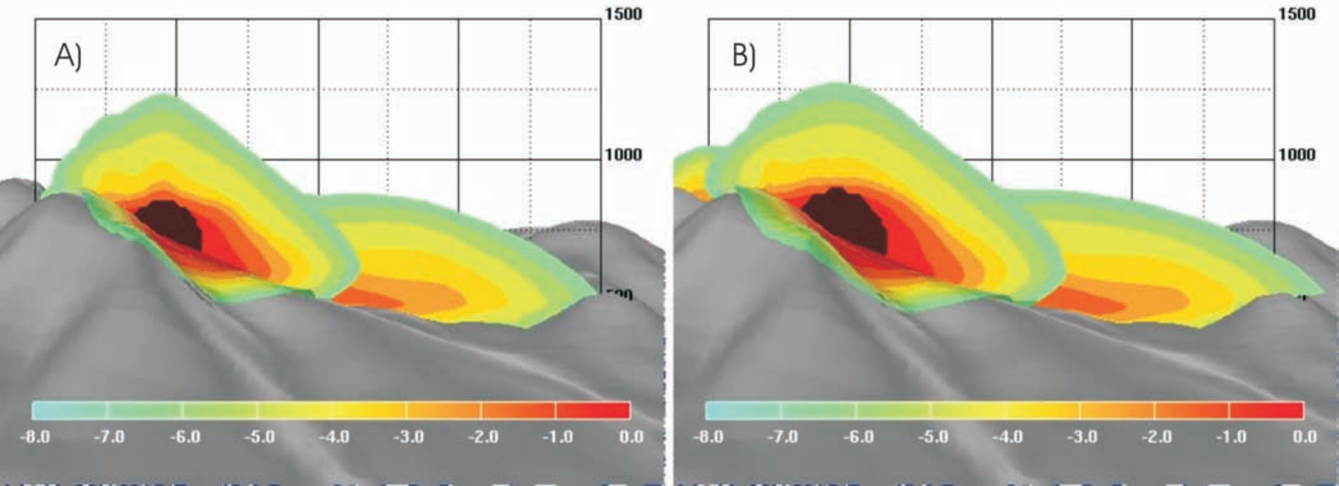
A)
1500
1000
500
-8.0
-7.0
-6.0
-5.0
-4.0
-3.0
-2.0
-1.0
0.0
B)
1500
1000
-8.0
-7.0
-6.0
-5.0
-4.0
-3.0
-2.0
-1.0
0.0

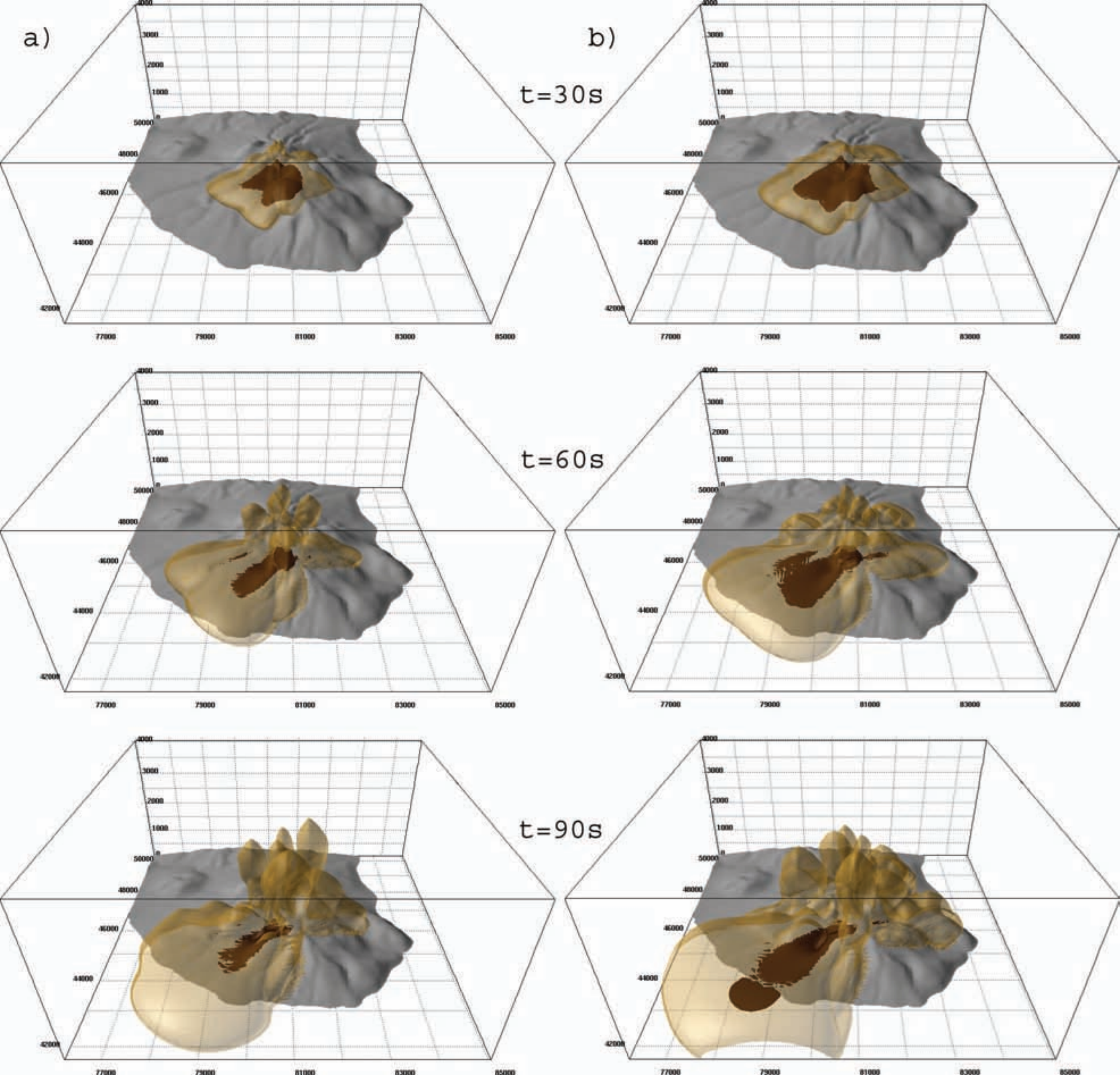
a)
b)
t=30s
t=60s
t=90s
4000
3000
2000
1000
0
50000
48000
46000
44000
42000
77000
79000
81000
83000
85000

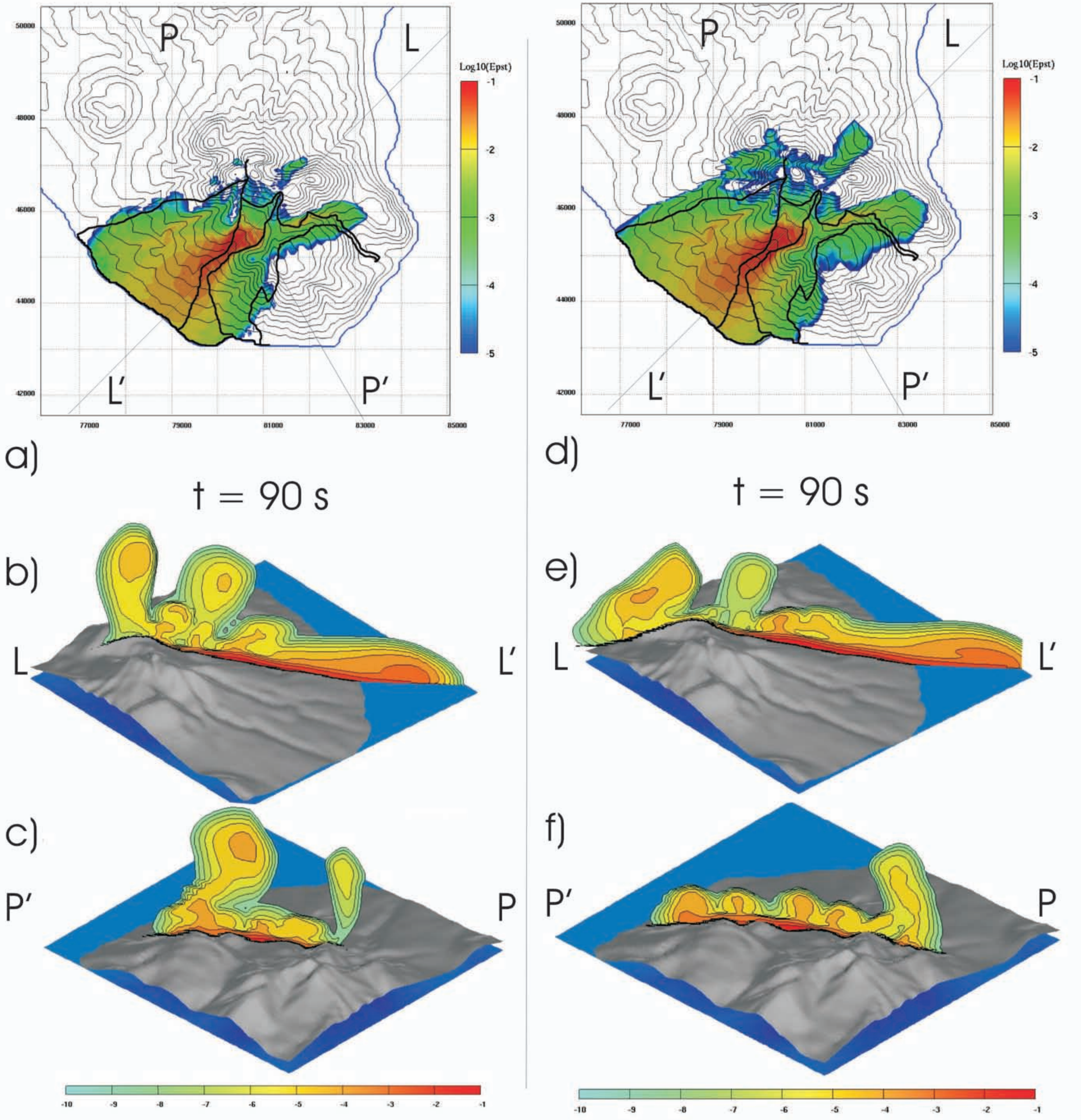
P
L
L′
P′
Log10(Epst)
-1
-2
-3
-4
-5
50000
48000
46000
44000
42000
77000
79000
81000
83000
85000
a)
d)
t = 90 s
t = 90 s
b)
e)
L
L′
c)
f)
P′
P
-10
-9
-8
-7
-6
-5
-4
-3
-2
-1

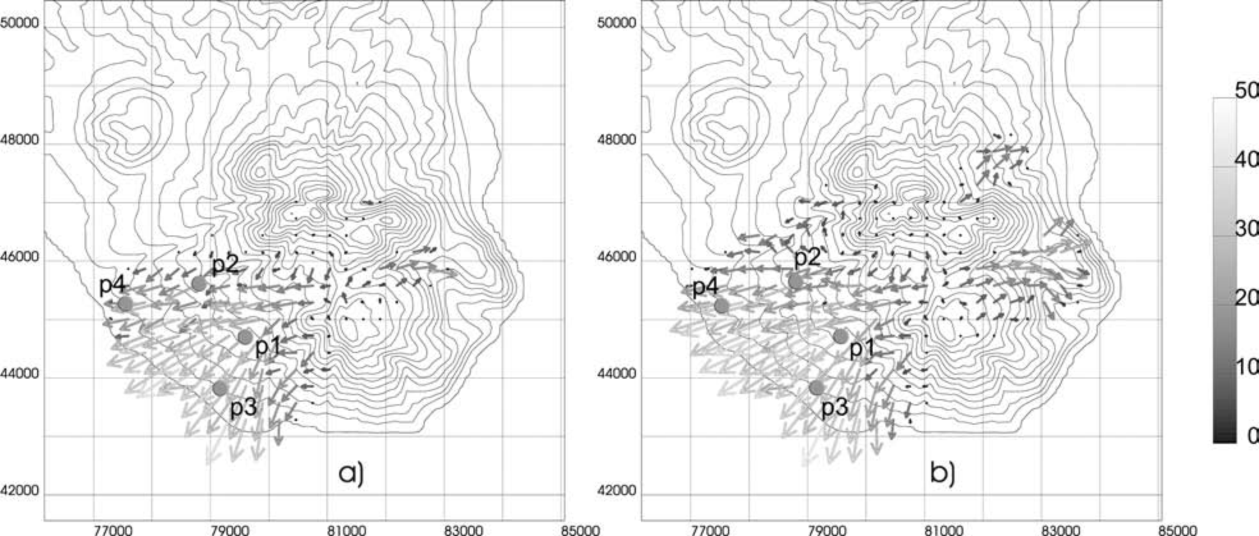
50000
48000
46000
44000
42000
77000
79000
81000
83000
85000
p1
p2
p3
p4
a)
b)
50
40
30
20
10
0

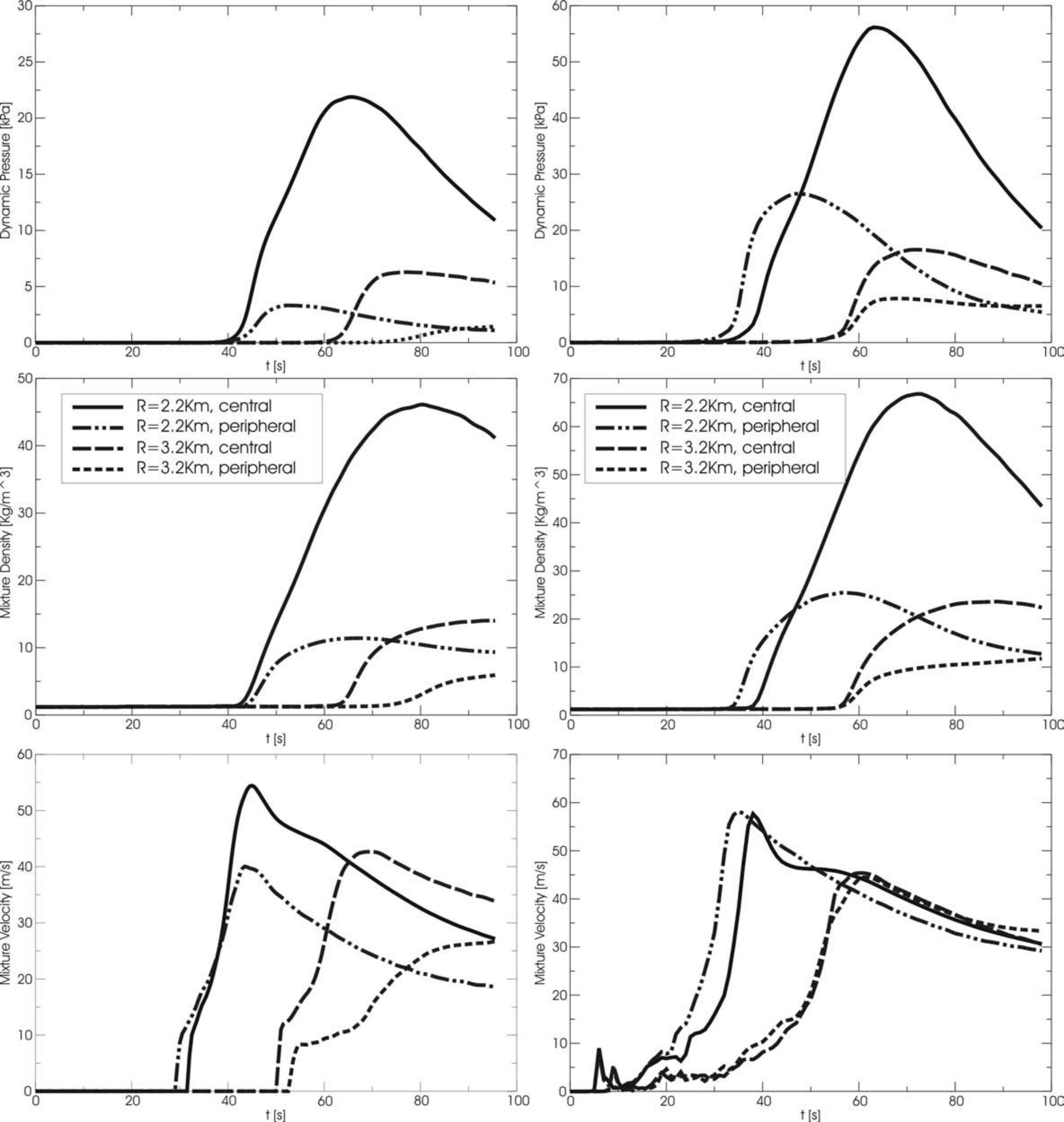
Dynamic Pressure [kPa]
Mixture Density [Kg/m ^ 3]
Mixture Velocity [m/s]
t [s]
R=2.2Km, central
R=2.2Km, peripheral
R=3.2Km, central
R=3.2Km, peripheral
0
20
40
60
80
100
0
5
10
15
20
25
30
40
50
60
70

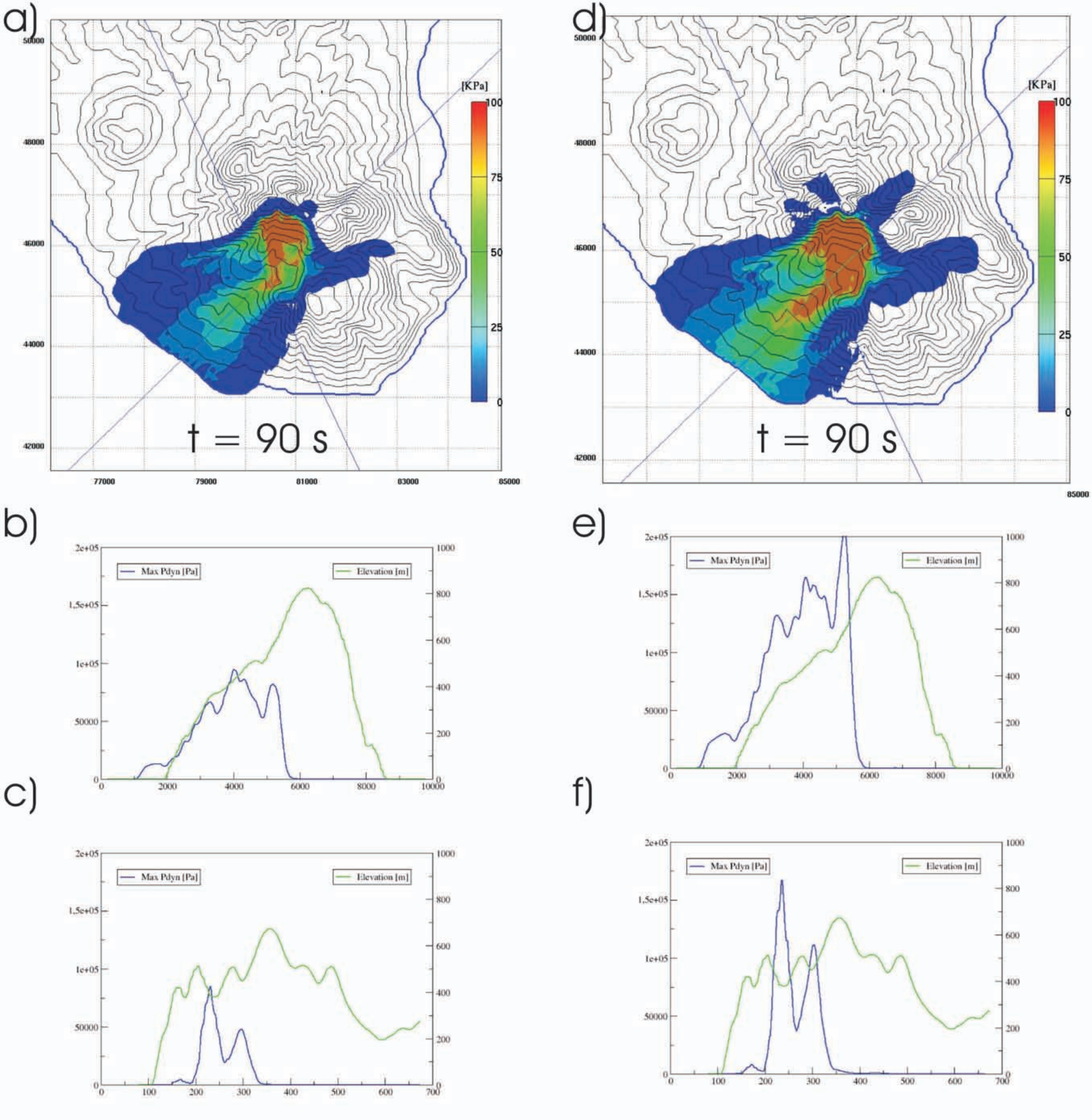
a)
50000
48000
46000
44000
42000
77000
79000
81000
83000
85000
[KPa]
100
75
50
25
0
t = 90 s
d)
50000
48000
46000
44000
42000
85000
[KPa]
100
75
50
25
0
t = 90 s
b)
Max Pdyn [Pa]
Elevation [m]
2e+05
1,5e+05
1e+05
50000
0
1000
800
600
400
200
0
0
2000
4000
6000
8000
10000
c)
Max Pdyn [Pa]
Elevation [m]
2e+05
1,5e+05
1e+05
50000
0
1000
800
600
400
200
0
0
100
200
300
400
500
600
700
e)
Max Pdyn [Pa]
Elevation [m]
2e+05
1,5e+05
1e+05
50000
0
1000
800
600
400
200
0
0
2000
4000
6000
8000
10000
f)
Max Pdyn [Pa]
Elevation [m]
2e+05
1,5e+05
1e+05
50000
0
1000
800
600
400
200
0
0
100
200
300
400
500
600
700

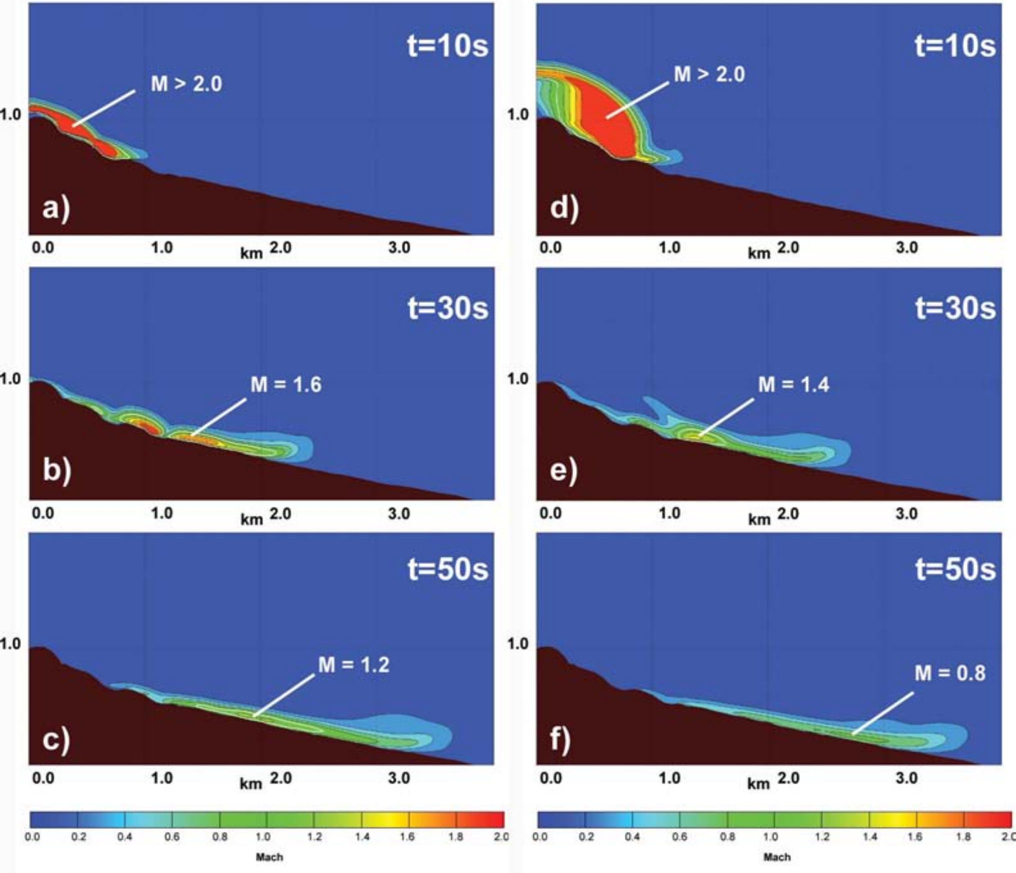
t=10s
M > 2.0
1.0
a)
0.0
1.0
km 2.0
3.0
t=10s
M > 2.0
1.0
d)
0.0
1.0
km 2.0
3.0
t=30s
M = 1.6
1.0
b)
0.0
1.0
km 2.0
3.0
t=30s
M = 1.4
1.0
e)
0.0
1.0
km 2.0
3.0
t=50s
M = 1.2
1.0
c)
0.0
1.0
km 2.0
3.0
t=50s
M = 0.8
1.0
f)
0.0
1.0
km 2.0
3.0
0.0 0.2 0.4 0.6 0.8 1.0 1.2 1.4 1.6 1.8 2.0
Mach
0.0 0.2 0.4 0.6 0.8 1.0 1.2 1.4 1.6 1.8 2.0
Mach

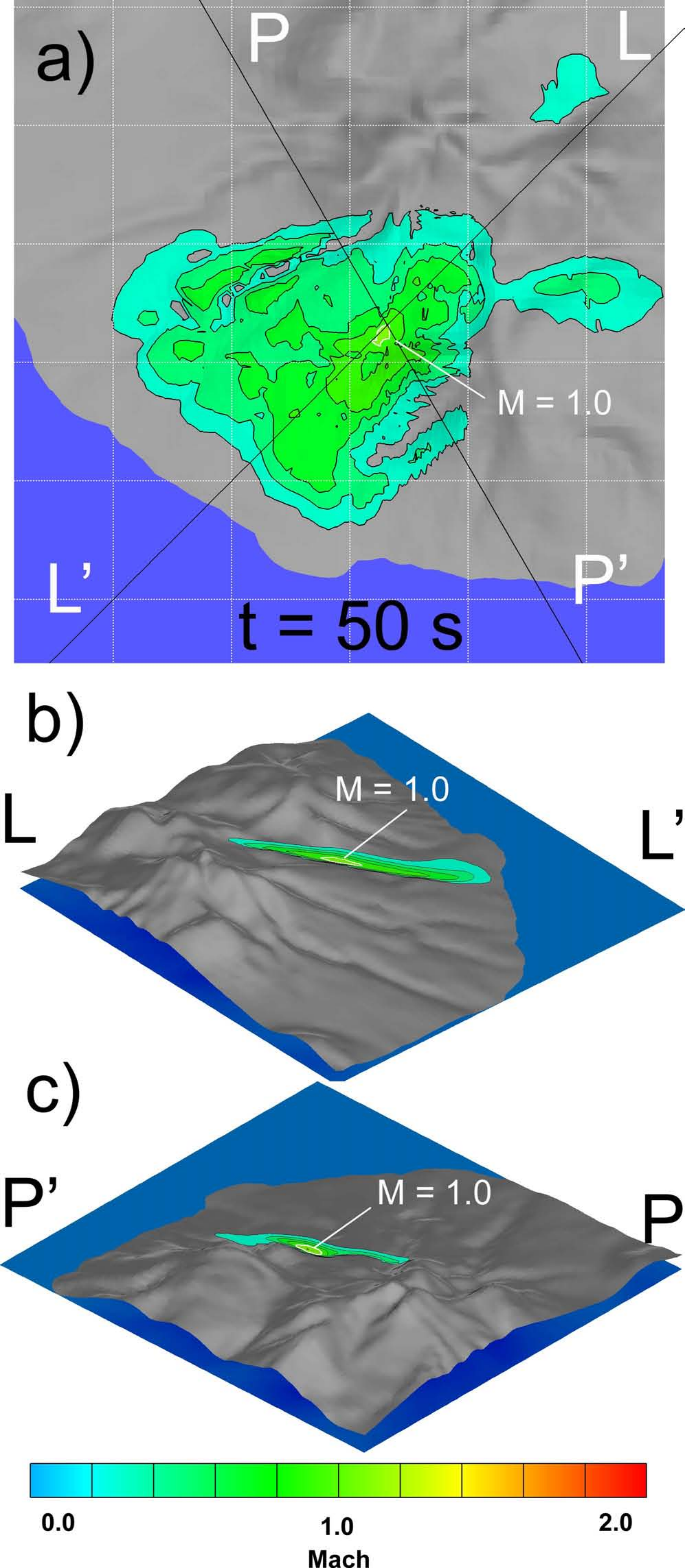
a)
P
L
M = 1.0
L'
P'
t = 50 s
b)
M = 1.0
L
L'
c)
M = 1.0
P'
P
0.0
1.0
2.0
Mach

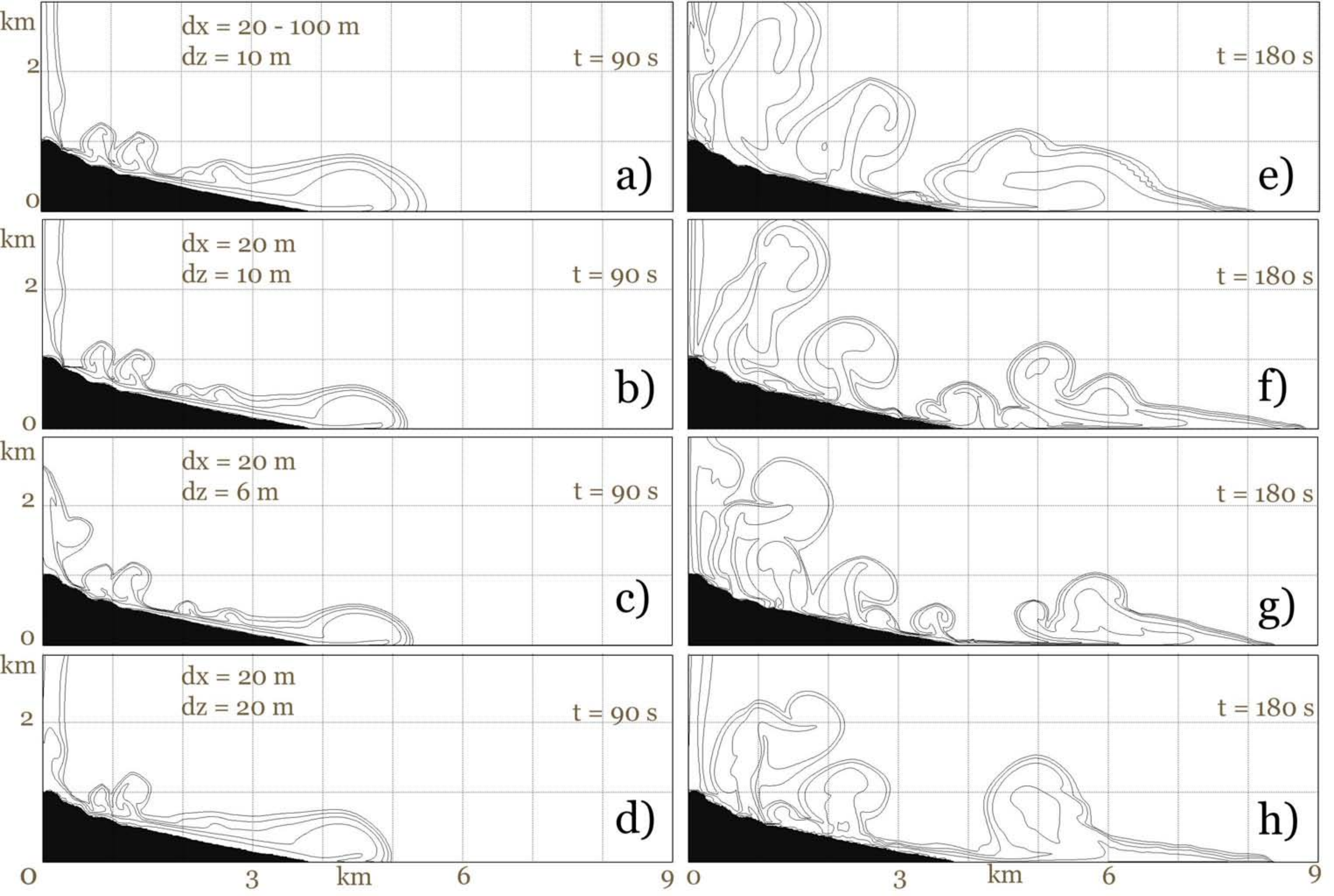
dx = 20 - 100 m
dz = 10 m
t = 90 s
a)
dx = 20 m
dz = 10 m
t = 90 s
b)
dx = 20 m
dz = 6 m
t = 90 s
c)
dx = 20 m
dz = 20 m
t = 90 s
d)
t = 180 s
e)
t = 180 s
f)
t = 180 s
g)
t = 180 s
h)
km
2
0
0
3
km
6
9

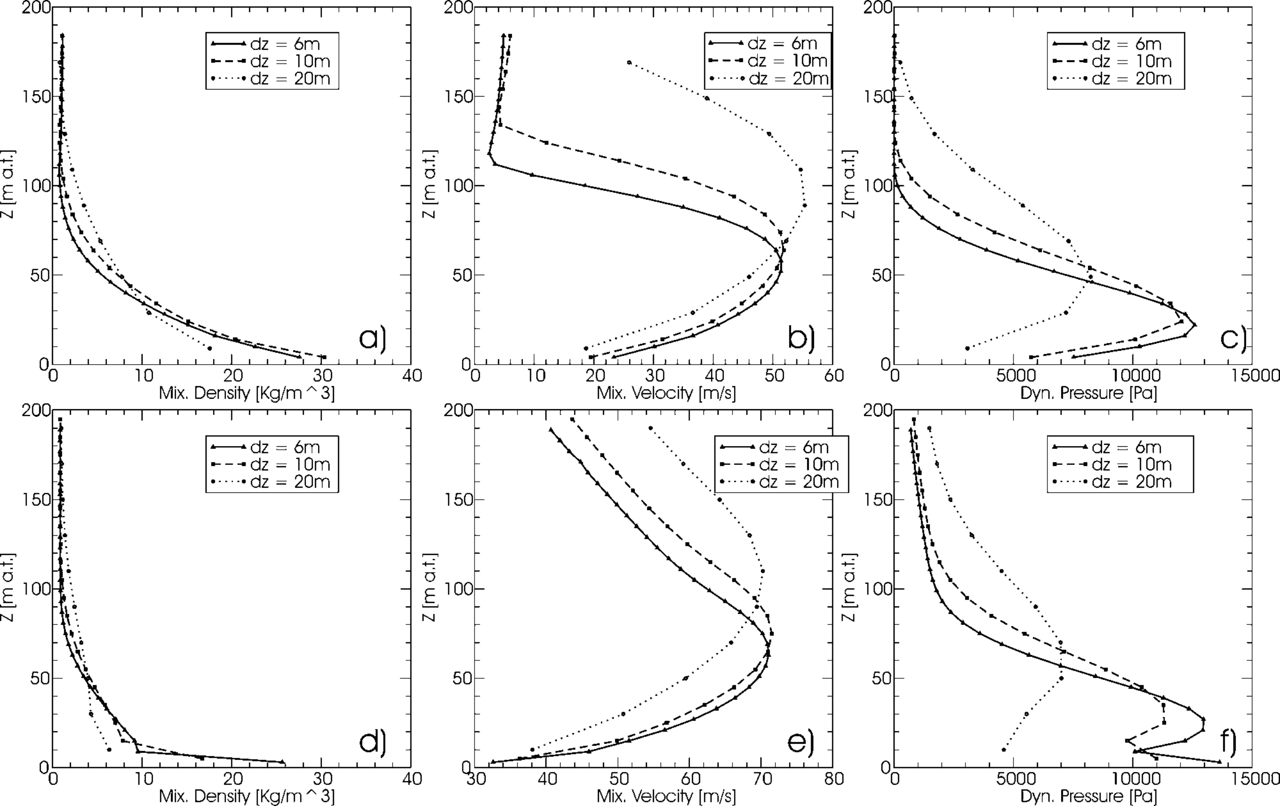
Z [m a.t.]
Mix. Density [Kg/m ^ 3]
Mix. Velocity [m/s]
Dyn. Pressure [Pa]
dz = 6m
dz = 10m
dz = 20m
a)
b)
c)
d)
e)
f)
0
50
100
150
200
0
10
20
30
40
50
60
70
80
5000
10000
15000

Run	κ(m^2)	V_{DRE} (m^3)	R_d (m)	Mass (kg)	α	E [J/kg]
A-2D	10^{-12}	5.0×10^6 $\times(360/70)$	227	60 x 10^9	0.1	320-490
B-2D	10^{-12}	10.0×10^6 $\times(360/70)$	280	120 x 10^9	0.1	390-610
C-2D	10^{-14}	5.0×10^6 $\times(360/70)$	227	60 x 10^9	0.1	1880-3380
A-3D	10^{-12}	5.0×10^6	142	12 x 10^9	0.1	320-480
B-3D	10^{-12}	10.0×10^6	180	24 x 10^9	0.1	340-520

Table 1

Run	H_b (m)	$U_{b,g}$ (m s^{-1})	$U_{b,p}$ (m s^{-1}) (5000, 500, 50µm)	U_f (m s^{-1})	T_p (s)	E (%) (5000, 500, 50 µm)	Rm_{max} (kg m^{-3}) (at 2,3,4 km)	Um_{max} (m s^{-1}) (at 2,3,4 km)	Pd_{max} (kPa) (at 2,3,4 km)	Pd_{SP} (kPa)
A-2D	250	160	75,125, 155	70	160	50, 20, ~0	57, 19, 18	46, 40, 34	44, 13, 7	>12.5
B-2D	300	160	75,125, 155	80	>180	0	54, 16, 17	72, 44, 33	46, 16, 6	>26
C-2D	500	175	85,145, 175	90	150	65, 30, <5	118, 38, 30	66, 43, 40	75, 28, 14	>14

Table2